# InSAR Phase Errors Due to Range Misregistrations

Fan Yang, Cunren Liang, and Yuhang Wang

***Abstract*—High-quality InSAR measurements require precise and accurate range coregistration both between the reference and the secondary synthetic aperture radar (SAR) images and between the reference SAR image and the digital elevation model (DEM) used for computing topographic phase. However, this requirement is not invariably satisfied due to the occurrence of range misregistrations. The range misregistration can occur between the reference image and the DEM, between the reference and secondary images, or due to the inhomogeneity within the range resolution cell. Our analysis reveals that, apart from the decorrelation effects, the effects of all three misregistration types ultimately reduce to that of an equivalent misregistration between the reference image and the DEM, which manifests as a phase error. Moreover, a closure phase error can be induced by the InSAR phase errors from the range misregistration between the reference and secondary images, as well as the inhomogeneity of the range resolution cell. We derive the InSAR and closure phase errors from both geometrical and signal theory perspectives, assuming a homogeneously distributed target. We further extend the derivation to different types of targets. The derived InSAR and closure phase errors are confirmed by simulation and real-data experiments.**

***Index Terms*—Closure phase, coregistration, range misregistration, synthetic aperture radar interferometry (InSAR).**

## I. Introduction

With the advancements in synthetic aperture radar (SAR) hardware and processing algorithms, both the precision and accuracy of SAR interferometry (InSAR) measurements have been substantially improved over the years. In the meantime, the SAR and InSAR processing workflows have become increasingly standardized. These developments call for a heightened focus on the *fine processing* of InSAR data to achieve further quality improvements and meet the requirements of new and emerging applications.

A critical prerequisite for the fine processing of InSAR data is range coregistration. This process involves the reference SAR image, the secondary SAR image, and the digital elevation model (DEM), which is used to compute and remove the topographic phase from the interferogram. During the coregistration of the latter two to the reference image, range misregistrations might occur. For the fine processing to yield high-quality measurements, these misregistrations must be constrained within a sufficiently small fraction of a resolution cell.

Received 3 October 2025; revised 29 November 2025, 19 January 2026, and 2 February 2026; accepted 9 February 2026. Date of publication 12 February 2026; date of current version 23 February 2026. This work was supported by the National Natural Science Foundation of China under Grant 42274026. *(Corresponding author: Cunren Liang.)*

The authors are with the Institute of Remote Sensing and Geographic Information System, School of Earth and Space Sciences, Peking University, Beijing 100871, China (e-mail: yangfan2018@pku.edu.cn; cunren.liang@pku.edu.cn; yh.wang@pku.edu.cn).

Digital Object Identifier 10.1109/TGRS.2026.3664181

Offsets between the reference image, and the DEM and secondary image arise from a combination of factors such as imaging geometry differences, atmospheric delays [1], [2], [3], [4], [5], [6], SAR system and processing errors [7], variations in scattering mechanisms, and resolution cell inhomogeneity. Most of these offsets are spatially inhomogeneous, with some varying rapidly at subresolution cell scales.

Three primary methods are currently employed to estimate offsets between the reference and secondary images, including cross correlation, spectral diversity [8] or multiple aperture InSAR (MAI) [9], and geometrical methods [10]. The geometrical method only accounts for the baseline-induced geometrical offset component, whereas cross correlation and spectral diversity methods estimate the full offset. While the geometrical method is inherently robust, the performances of cross correlation and spectral diversity methods are limited by interferometric coherence [11]. Consequently, none of these methods can universally guarantee the estimation of spatially varying offsets with consistently high precision and accuracy, inevitably leading to residual misregistrations.

Azimuth misregistration between reference and secondary images has attracted considerable interest in recent years. This is largely due to the prevalent adoption of burst mode in current SAR satellites, including the TOPS mode of Sentinel-1 and ScanSAR mode of ALOS-2 [12], [13]. The major concern centers on the InSAR phase bias that is jointly induced by the azimuth misregistration and the large Doppler centroid frequencies present at burst edges [8], [13], [14], [15].

The range misregistration, by contrast, has been largely overlooked. Previous research has predominantly investigated the effects of range misregistrations from a statistical perspective, concentrating on the resulting decorrelation [16], [17]. In practice, a misregistration threshold of 0.1 resolution cell has become a widely adopted standard to ensure that decorrelation effects remain acceptable. This requirement was originally proposed based on the decorrelation effects on the standard deviation of the InSAR phase, which is an indicator of measurement precision.

High-quality InSAR measurements require not only high precision but also high accuracy. Accuracy specifically requires that the expectation of the measurement error, or the bias, be minimized. As this article will demonstrate, a range misregistration introduces not only decorrelation noise but also a systematic phase bias undermining accuracy. While the phase bias induced by azimuth misregistrations in burst mode data processing has been extensively investigated [8], [13], [14], [15], the phase bias (hereafter referred to as InSAR phase error) due to range misregistrations remains unexamined.

1558-0644 © 2026 IEEE. All rights reserved, including rights for text and data mining, and training of artificial intelligence and similar technologies. Personal use is permitted, but republication/redistribution requires IEEE permission.
See https://www.ieee.org/publications/rights/index.html for more information.
Authorized licensed use limited to: Peking University. Downloaded on March 05,2026 at 17:19:39 UTC from IEEE Xplore. Restrictions apply.

In this article, we investigate the range misregistration and find: 1) a range misregistration, whether between the reference image and the DEM or between the reference and secondary images, induces an InSAR phase error, in addition to the previously known decorrelation noise; and 2) the InSAR phase error due to the range misregistrations between the reference and secondary images would further give rise to a nonzero InSAR closure phase (hereafter referred to as closure phase error) [18], [19]. Similarly, the inhomogeneity of the range resolution cell can also generate a closure phase error. Unlike the closure phase of physical origins that has been primarily investigated in previous works [19], [20], [21], [22], this newly discovered closure phase error stems from data processing inaccuracies. It would affect all problems associated with the closure phase, including its direct application as an observable and its role in affecting measurements from InSAR stack processing.

The remainder of this article is organized as follows. Section II reviews the known sources of range offsets in InSAR and the commonly used estimation methods, along with the resulting errors. Section III summarizes the mechanisms underlying the InSAR and closure phase errors due to range misregistrations. Section IV formulates these InSAR and closure phase errors and introduces the correction methods. Validations through simulated and real-data experiments are presented in Sections V and VI, respectively. Finally, this article concludes with a summary in Section VII.

## II. Range Offsets in InSAR and Their Estimation Methods

### A. Overview of Known Range Offsets in InSAR

The range bandwidth of a spaceborne SAR system typically spans from 10 to 100 MHz, which corresponds to a range resolution between approximately 1.50 and 14.99 m. According to the Nyquist sampling theorem, the actual range pixel size is slightly reduced by a factor equal to the oversampling ratio. A variety of sources can induce range offsets that vary both temporally and spatially, with magnitudes that may exceed or be comparable to the size of a range resolution cell or pixel.

The spatial baseline between SAR acquisitions constitutes the primary source of range offset in InSAR. Under current satellite orbit configurations, such geometrical offsets typically vary from several meters to several hundred meters. Terrestrial surface motions also introduce signal path differences that manifest as range offsets in SAR data. Such motions can result from crustal movements (mm/yr to cm/yr), tidal and loading effects (mm to dm), anthropogenic activities (mm/yr to m/yr), earthquakes and volcanoes (cm to m), and glaciers (m/yr to km/yr), among others.

Atmospheric refraction of microwave signals is another significant source of range offset, leading to propagation delays through the atmosphere. Tropospheric delay comprises two principal components: a relatively larger but temporally stable dry delay, and a smaller yet highly variable wet delay [23]. Under typical meteorological conditions at sea level, the zenith dry delay approximates 2.3 m, whereas the zenith wet delay ranges from several millimeters in polar regions to approximately 40 cm in equatorial zones [24]. In contrast to the troposphere, the ionosphere behaves as a dispersive medium for microwave signals, with its induced delay inversely proportional to the square of the signal frequency [25]. The ionospheric delay can reach several meters at C-band and tens of meters at L-band. Fig. 1 shows three representative examples of substantial range offsets resulting from ionospheric delays.

In addition to the aforementioned range offsets, variations in ground scattering mechanisms can also induce range offsets comparable in magnitude to the range pixel size. This phenomenon has been widely observed in C-band Sentinel-1 data in vegetated areas [26]. A representative example from L-band ALOS-2 data is presented in Fig. 2.

Range offsets may also originate from the SAR system and processing errors. For example, the precision of near range measurements is critically dependent on geometrical calibration precision [27]. In ALOS-2 products, the near range value is stored as an integer in meters, and its error can exceed a pixel for ScanSAR mode (range pixel size: 8.6 m) in early products [28]. Fig. 1(c) shows a couple of commonly observed range offsets in Sentinel-1 TOPS data, which are likely attributed to SAR system and processing errors. Among these, the offset errors in rectangular chunks may result from the assumptions adopted in secondary range focusing [29].

The range offsets induced by spatial baselines, terrestrial surface motions, and atmosphere appear in both amplitude and phase with equal magnitude. However, the range offsets induced by the ionosphere exhibit opposite signs in amplitude and phase, given that the ionosphere causes a phase advance instead of a delay. For the range offsets induced by variations in ground scattering mechanisms and SAR system and processing errors, however, an amplitude offset is not necessarily accompanied by a phase offset. Moreover, such offsets are also not necessarily spatially smooth, which makes their estimation quite challenging.

It should be noted that the range offsets discussed above may not represent an exhaustive catalog. They constitute only a subset of range offset types that have been identified.

### B. Range Offset Estimation Methods and Resulting Errors

Three principal methods are commonly employed for estimating offsets between a pair of SAR images, including cross correlation, spectral diversity [8], [9], and geometrical methods [10]. Each of them is applicable to the estimation of range offsets.

Of the three principal methods, the geometrical method is typically applied first in state-of-the-art InSAR workflows to estimate offsets induced by spatial baseline. This method uses the well-established range Doppler equations to compute the offsets [10]. Required inputs include near ranges, azimuth starting times, orbits (time, position, and velocity), and a DEM. For representative modern satellites, orbit errors are typically on the order of a few centimeters, rendering their impact on offset estimation nearly negligible. The errors in the computed range offsets are mainly given as follows.

1) Range offset errors due to DEM errors. These errors exhibit significant spatial variability. Currently, high-precision

Authorized licensed use limited to: Peking University. Downloaded on March 05,2026 at 17:19:39 UTC from IEEE Xplore. Restrictions apply.

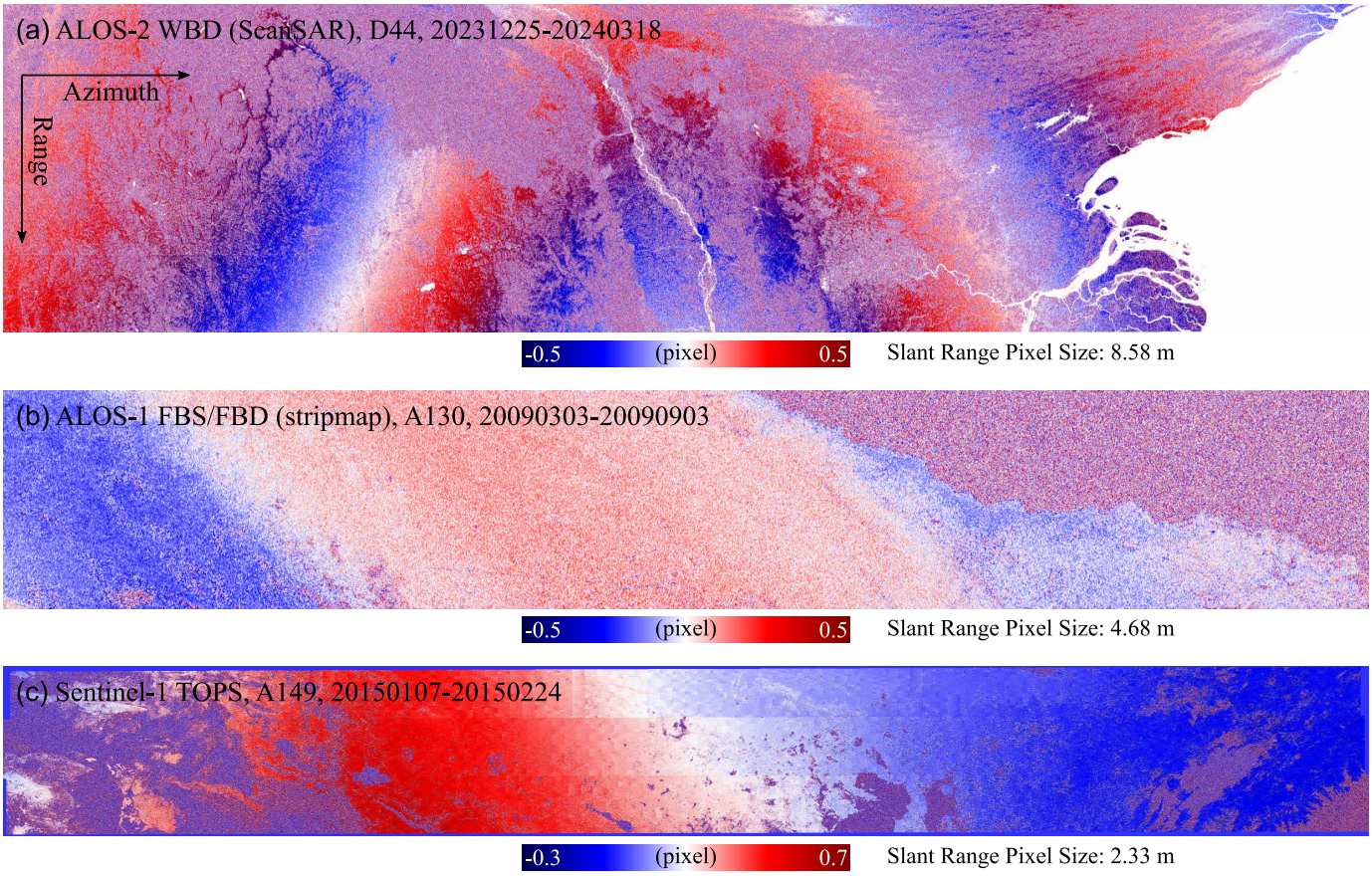


Fig. 1. Large InSAR range offsets resulting from microwave refraction in the ionosphere. Geometrical range offsets caused by the spatial baseline have been removed prior to estimating these offsets using the cross correlation method. (a) Region extending from Tibet, China, to South Asia. (b) Region in northern Chile. (c) Region predominantly in northern Chile. In addition to the background range offsets due to ionosphere, (c) also exhibits patterns that are likely associated with systematic and processing errors, including offset errors in rectangular chunks and relative offset errors between swaths.

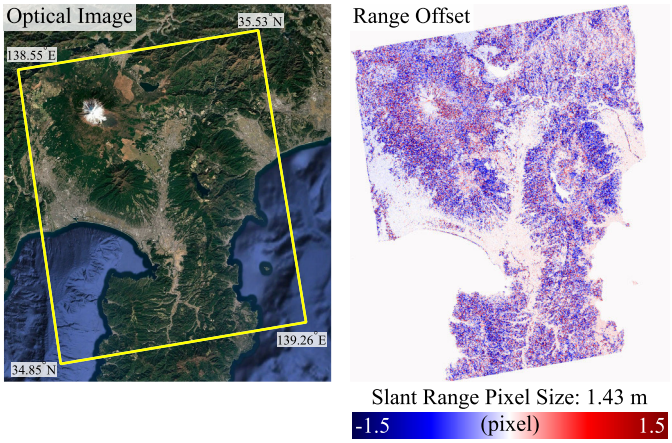


Fig. 2. InSAR range offsets induced by vegetation at L-band. Geometrical range offsets caused by the spatial baseline have been removed prior to estimating this offset using the cross correlation method. Data: ALOS-2 UBS (Stripmap) mode, track A126, pair 2019/06/21-2024/05/31.

global DEMs, such as SRTM 30-m DEM with a precision better than 9.0 m [30], TanDEM-X 30 m EDEM with 3.49-m precision [31], and Copernicus 30-m DEM with 2.17-m precision [32], are available. With orbit tubes of most modern satellites maintained within 500 m, range offset errors due to DEM errors are generally negligible [10]. However, in rugged topography, these DEM errors can become substantial.

2) Range offset errors due to near range errors. These errors mainly manifest as a spatially invariant bias across the entire image.

Following the application of the geometrical method, which corrects for range offsets induced by spatial baseline, residual offsets persist. These include spatially varying offsets from other sources, as well as a constant residual offset set in 2). Even after implementing the corrections suggested in [33], the residual offsets might still be significant. Therefore, the cross correlation or spectral diversity method should be applied to estimate these remaining range offsets, preferably using the SLC images after geometrical coregistration. The cross correlation method additionally uses texture information beyond speckle tracking, thereby making it more robust against decorrelation. Considering the operational complexity associated with implementing the spectral diversity method, the cross correlation method is preferred in practical applications.

Current software packages do not mandate the estimation of residual range offsets following geometrical correction [34], [35], [36]. Consequently, certain implementations rely exclusively on the geometrical method, which may result in substantial range misregistrations between the reference and secondary images. Some workflows use the cross correlation

Authorized licensed use limited to: Peking University. Downloaded on March 05,2026 at 17:19:39 UTC from IEEE Xplore. Restrictions apply.

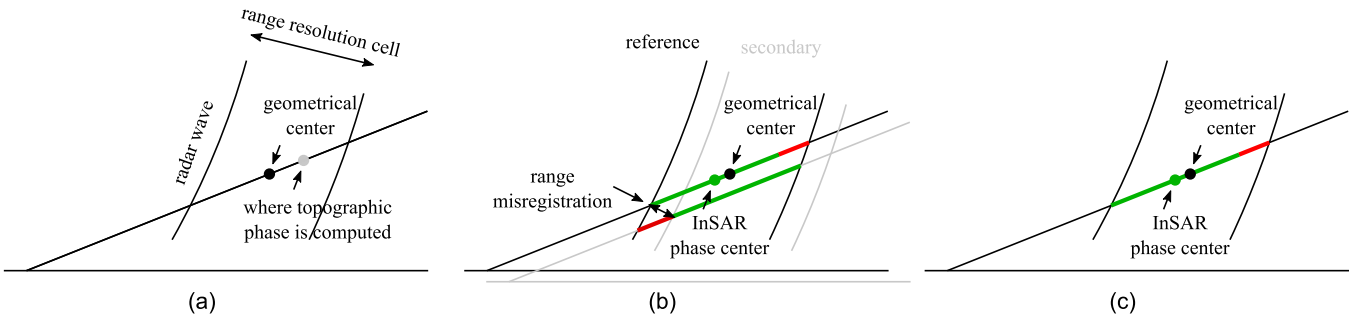


Fig. 3. (a) Range misregistration between reference SAR image and DEM. (b) Range misregistration between reference and secondary SAR images. The reference and secondary acquisitions are indicated in black and gray, respectively. Green and red lines denote the same and different scatterers within the coregistered range resolution cell. (c) Range misregistration resulting from inhomogeneity within the resolution cell.

method to estimate only a constant residual offset across the entire image, thereby neglecting the spatially varying components. A polynomial model or even an offset field would more accurately represent these spatially varying components, albeit at the cost of reduced robustness as model complexity increases.

In practice, neither cross correlation nor spectral diversity method can consistently and accurately estimate the full spatially varying range offset field, e.g., the one in Fig. 2, as their performances are inherently limited by coherence [11].

As noted in Section II-A, the range offset due to spatial baseline also manifests in the InSAR phase. Therefore, the range offset computed by the geometrical method is used to remove the topographic phase. However, the reference SAR image itself contains distortions from spatially varying range offsets relative to the DEM. The difficulty in precisely estimating these offsets results in a residual topographic phase, as will be analyzed in Section III.

## III. Underlying Mechanism

Here, our discussion is limited to the range direction. For simplicity, we assume a homogeneously distributed target. We begin with the scenario of a misregistration between the reference SAR image and the DEM, as illustrated in Fig. 3(a). The InSAR phase center of a range resolution cell lies at its geometrical center. In the absence of misregistration, the topographic phase, which is computed solely from the imaging geometry at the geometrical center and is independent of the SAR images, can be regarded as accurate if errors in orbit and DEM data are negligible [10]. The presence of the misregistration, however, which is common in practical data processing, equates to computing the topographic phase at a position different from the geometrical center, thereby leaving a residual topographic phase after the computed topographic phase is removed.

In the presence of a range misregistration between reference and secondary SAR images, as illustrated in Fig. 3(b), the corresponding range resolution cell of each image—bounded by the two black lines—contains two groups of scatterers represented by the green and red lines. The scatterers marked in green are common to both reference and secondary resolution cells, signifying the same ground scatterers. In contrast, those marked in red are unique to each image, representing different scatterers. These distinct scatterers are incoherent; therefore, their contributions in the interferogram constitute noise rather than a signal. Consequently, the InSAR phase center shifts to the geometrical center of the common (green) scatterers, which is only a portion of the original resolution cell. The topographic phase, however, is still computed based on the geometrical center of the full, original resolution cell. This discrepancy, analogous to the case in Fig. 3(a), gives rise to a residual topographic phase. However, this phase bias has been neglected in previous work, which concentrated exclusively on the decorrelation noise [16], [17]. In summary, the overall effects of this misregistration include a residual phase error and decorrelation noise.

As will be discussed in Section IV, the residual topographic phase is proportional to the product of the misregistration and perpendicular baseline (or range frequency shift). In the context of multiple images, e.g., a stack, the misregistration depicted in Fig. 3(a) remains constant for a given range resolution cell across all InSAR pairs. Since the misregistration is a common factor and the perpendicular baselines sum to zero in a closed loop, no closure phase is produced. However, in the case of Fig. 3(b), the misregistration tends to vary for different InSAR pairs. Consequently, the coupling between these misregistrations and perpendicular baselines leads to a nonzero closure phase.

In the third scenario, illustrated in Fig. 3(c), the scatterers represented by the red line decorrelated between repeat-pass acquisitions, leaving only the green scatterers correlated. This renders the resolution cell effectively inhomogeneous for InSAR processing. Consequently, the resulting effects are similar to those of Fig. 3(b). Moreover, variation in which scatterers decorrelate across different InSAR pairs can potentially lead to a nonzero closure phase. Furthermore, if scatterers with different reflectivities are distributed nonuniformly within the resolution cell, the InSAR phase center also deviates from its geometrical center, resulting in a residual topographic phase.

To summarize, while the first case [Fig. 3(a)] introduces solely a residual topographic phase, the latter two cases [Fig. 3(b) and (c)] yield identical effects: a residual topographic phase, decorrelation, and a nonzero closure phase. Since the second case is representative and manifests all these effects, it will serve as the framework for quantifying them in Section IV.

Authorized licensed use limited to: Peking University. Downloaded on March 05,2026 at 17:19:39 UTC from IEEE Xplore. Restrictions apply.

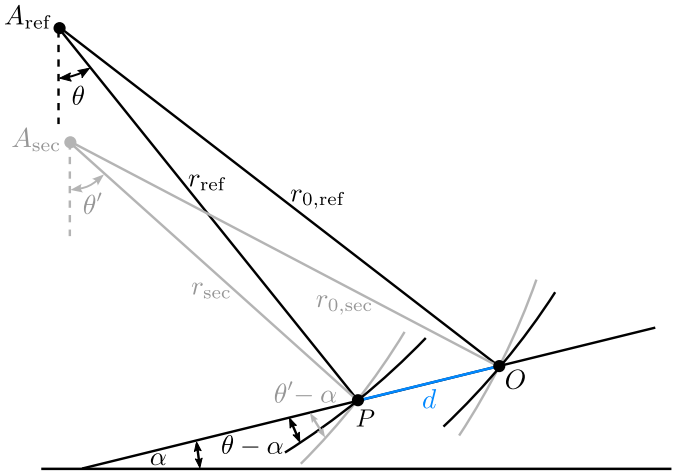


Fig. 4. InSAR geometry.

## IV. Effects of a Misregistration Between Reference and Secondary SAR Images

### A. InSAR Geometry and Topographic Phase

The InSAR geometry is illustrated in Fig. 4. For simplicity, we adopt a rectilinear imaging geometry with a smooth ground surface of constant slope $\alpha$. The antenna phase centers of the reference and secondary image, denoted as $A_{\text{ref}}$ and $A_{\text{sec}}$, correspond to look angles of $\theta$ and $\theta' = \theta + \Delta\theta$, respectively.

Assume that a resolution cell on the ground surface has a geometrical center $O$. The slant ranges from the antenna phase centers to $O$ are $r_{0,\text{ref}}$ and $r_{0,\text{sec}}$. The difference between the two slant ranges at $O$ defines the parallel baseline expressed as $b_r = r_{0,\text{ref}} - r_{0,\text{sec}}$. Let $P$ be an arbitrary point within the resolution cell, located at a small distance $d$ from $O$. The slant ranges from the antenna centers to $P$ are $r_{\text{ref}}$ and $r_{\text{sec}}$. Our purpose now is to determine the slant range difference at $P$, defined as $\Delta r_P = r_{\text{ref}} - r_{\text{sec}}$, and the corresponding InSAR phase $\varphi_P = -4\pi f_0 \Delta r_P / c$, where $f_0$ denotes the radar center frequency and $c$ is the speed of light.

As illustrated in Fig. 4, the angle between the ground surface and the reference radar wavefront at $P$ is $\theta - \alpha$. By considering triangle $A_{\text{ref}}PO$, the difference between the two slant ranges $r_{\text{ref}}$ and $r_{0,\text{ref}}$ is

$$r_{\text{ref}} - r_{0,\text{ref}} = -d \sin(\theta - \alpha). \tag{1}$$

For the secondary radar wavefront, the angle becomes $\theta' - \alpha$. Similarly, by considering the triangle $A_{\text{sec}}PO$, the difference of the two slant ranges $r_{\text{sec}}$ and $r_{0,\text{sec}}$ is

$$\begin{aligned} r_{\text{sec}} - r_{0,\text{sec}} &= -d \sin(\theta' - \alpha) \\ &= (r_{\text{ref}} - r_{0,\text{ref}}) \frac{\sin(\theta' - \alpha)}{\sin(\theta - \alpha)} \\ &\approx (r_{\text{ref}} - r_{0,\text{ref}}) \frac{\sin(\theta - \alpha) + \cos(\theta - \alpha)\Delta\theta}{\sin(\theta - \alpha)} \\ &= (r_{\text{ref}} - r_{0,\text{ref}}) \left[1 + \frac{\Delta\theta}{\tan(\theta - \alpha)}\right]. \end{aligned} \tag{2}$$

Combining these results, the slant range difference at $P$ can be expressed as

$$\begin{aligned} \Delta r_P &= r_{\text{ref}} - r_{\text{sec}} \\ &= (r_{\text{ref}} - r_{0,\text{ref}}) - (r_{\text{sec}} - r_{0,\text{sec}}) + r_{0,\text{ref}} - r_{0,\text{sec}} \\ &= (r_{\text{ref}} - r_{0,\text{ref}}) - (r_{\text{ref}} - r_{0,\text{ref}}) \left[1 + \frac{\Delta\theta}{\tan(\theta - \alpha)}\right] + b_r \\ &= b_r - \frac{\Delta\theta}{\tan(\theta - \alpha)} (r_{\text{ref}} - r_{0,\text{ref}}). \end{aligned} \tag{3}$$

Accordingly, the corresponding InSAR phase at $P$ is

$$\begin{aligned} \varphi_P &= -\frac{4\pi f_0}{c} \Delta r_P \\ &= \frac{4\pi f_0}{c} \left[-b_r + \frac{\Delta\theta}{\tan(\theta - \alpha)} (r_{\text{ref}} - r_{0,\text{ref}})\right] \\ &= \frac{4\pi}{c} \left[-f_0 b_r + \Delta f (r_{\text{ref}} - r_{0,\text{ref}})\right] \end{aligned} \tag{4}$$

where $\Delta f = f_0 \Delta\theta / \tan(\theta - \alpha) \approx f_0 b_p / [r_{0,\text{ref}} \tan(\theta - \alpha)]$ is the range frequency shift found in [37] and $b_p$ is the perpendicular baseline between the antenna phase centers.

### B. InSAR Phase Error Due to Range Misregistration

Here, we derive the InSAR phase error geometrically. A resolution cell on the ground is considered to comprise numerous independent homogeneous elementary scatterers, neglecting mutual interactions. The total scattered electromagnetic wave from the resolution cell is the superposition of the waves scattered by all elementary scatterers. By conceptualizing the resolution cell as analogous to a SAR antenna consisting of multiple radiating elements, it follows that the resolution cell has an effective phase center.

The interferometric signal is generated exclusively by scatterers present in both the reference and secondary resolution cells. Assume that $r_{0,\text{ref}}$ is the slant range at the geometrical center of the resolution cell in the reference image and $b_r$ represents the parallel baseline. Provided that the secondary image is well coregistered to the reference image, the InSAR phase center will coincide with the geometrical center. However, when a range misregistration $r_{\text{mis}}$ is present between the reference and secondary images, the InSAR phase center is displaced to the geometrical center of the common part of the two resolution cells, e.g., the parts of resolution cells in green in Fig. 3(b), and the associated slant range $\tilde{r}$ is

$$\tilde{r} = r_{0,\text{ref}} + \frac{r_{\text{mis}}}{2}. \tag{5}$$

According to (4), the InSAR phase at the phase center is

$$\begin{aligned} \tilde{\varphi} &= \frac{4\pi}{c} \left[-f_0 b_r + \Delta f (\tilde{r} - r_{0,\text{ref}})\right] \\ &= \frac{4\pi}{c} \left(-f_0 b_r + \Delta f \frac{r_{\text{mis}}}{2}\right). \end{aligned} \tag{6}$$

The InSAR phase at the geometrical center is

$$\varphi_0 = -\frac{4\pi}{c} f_0 b_r. \tag{7}$$

The phase error due to the misregistration is thus given by the difference between the InSAR phases at the phase center and geometrical center of the resolution cell

$$\begin{aligned} \varphi_{\text{error}} &= \tilde{\varphi} - \varphi_0 \\ &= \frac{4\pi}{c} \left[-f_0 b_r + \Delta f (\tilde{r} - r_{0,\text{ref}})\right] - \left(-\frac{4\pi}{c} f_0 b_r\right) \end{aligned}$$

Authorized licensed use limited to: Peking University. Downloaded on March 05,2026 at 17:19:39 UTC from IEEE Xplore. Restrictions apply.

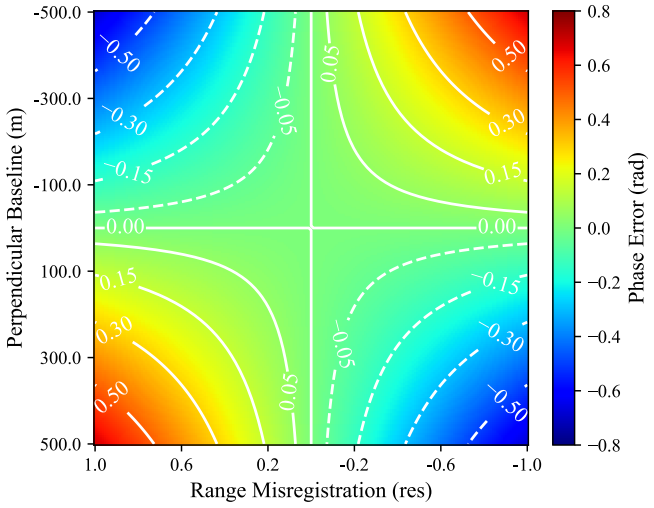


Fig. 5. InSAR phase errors due to the range misregistrations between reference and secondary SAR images. The radar center frequency is 1.26 GHz. The range resolution is 10.71 m. The look angle is 35°. The ground slope is 20°.

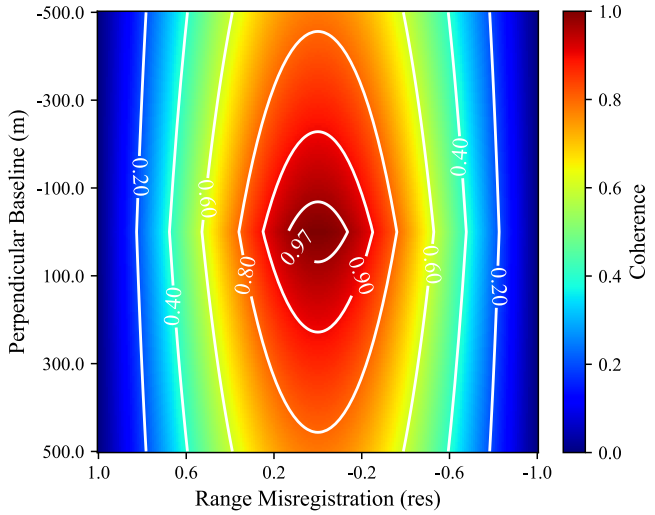


Fig. 6. Decorrelation in (11). The radar center frequency is 1.26 GHz. The range resolution is 10.71 m. The look angle is 35°. The ground slope is 20°.

$$= \frac{4\pi}{c}\Delta f\left(\tilde{r} - r_{0,\text{ref}}\right) = \frac{4\pi}{c}\Delta f\frac{r_{\text{mis}}}{2} = 2\pi\Delta f\frac{t_{\text{mis}}}{2} \tag{8}$$

where $t_{\text{mis}} = 2r_{\text{mis}}/c$ is the range misregistration in seconds.

A more in-depth derivation of the InSAR phase error from a signal theory perspective is provided in the Appendix, leading to the same result.

The InSAR phase errors computed under typical configurations are shown in Fig. 5.

### C. Decorrelation Due to Range Misregistration

Having established the analytical framework in the Appendix, we now compute the decorrelation due to range misregistration. From (33), the expected amplitude of the interferogram is

$$W_I = \bar{\sigma}\frac{\sin\left[\pi t_{\text{mis}}\left(|K|T - |\Delta f|\right)\right]}{\pi t_{\text{mis}}} \tag{9}$$

where $\bar{\sigma}$ is the radar cross section (RCS) density in range, $K$ is the range chirp rate, $T$ is the range chirp duration, and $|K|T$ is the SAR signal bandwidth. As $\Delta f$ is the range frequency shift, $|K|T - |\Delta f|$ is the effective range bandwidth for generating the interferometric signal.

Letting $t_{\text{mis}} = 0$ and $\Delta f = 0$, the expected intensities of the SAR images are

$$W_{\text{ref}} = W_{\text{sec}} = \bar{\sigma}|K|T. \tag{10}$$

Therefore, the coherence of the interferogram can be expressed as

$$\rho = \frac{W_I}{\sqrt{W_{\text{ref}}W_{\text{sec}}}} = \frac{|K|T - |\Delta f|}{|K|T}\frac{\sin\left[\pi t_{\text{mis}}\left(|K|T - |\Delta f|\right)\right]}{\pi t_{\text{mis}}\left(|K|T - |\Delta f|\right)} = \rho_{\text{geom}}\rho_{\text{mis}}. \tag{11}$$

The first term, $\rho_{\text{geom}} = (|K|T - |\Delta f|)/(|K|T)$, is the geometrical decorrelation, and the second term, $\rho_{\text{mis}} = \sin[\pi t_{\text{mis}}(|K|T - |\Delta f|)]/[\pi t_{\text{mis}}(|K|T - |\Delta f|)] = \text{sinc}[t_{\text{mis}}(|K|T - |\Delta f|)]$, is the decorrelation due to range misregistration as that derived in [16].

The decorrelation resulting from typical configurations is presented in Fig. 6, using the same parameter set as in Fig. 5.

### D. InSAR Phase Error for Different Types of Targets

Here, we generalize the InSAR phase error model in (8) to accommodate different target types. Let us consider a range resolution cell with an InSAR phase center located at $\tilde{r}$, which depends on the target type, and a geometrical center $r_{0,\text{ref}}$. From (8), the InSAR phase error is

$$\varphi_{\text{error}} = \frac{4\pi}{c}\Delta f\left(\tilde{r} - r_{0,\text{ref}}\right). \tag{12}$$

We consider three types of targets within the range resolution cell.

1) A target consisting of a single scatterer, which is known as a persistent scatterer (PS).

2) A distributed target, modeled as in Section IV-B by a large number of elementary scatterers. Each elementary scatterer is an independent, zero-mean complex Gaussian variable with a common variance.

3) A mixed target that is intermediate between 1) and 2): the target contains one dominant scatterer in addition to a large number of elementary scatterers, as described in 2).

For a type 1) target, the InSAR phase center is located at the scatterer's position $\tilde{r}_{\text{PS}}$. Consequently, the phase error is proportional to the range difference between this position and the geometrical center of the range resolution cell

$$\varphi_{\text{error}}^{\text{PS}} = \frac{4\pi}{c}\Delta f\left(\tilde{r}_{\text{PS}} - r_{0,\text{ref}}\right). \tag{13}$$

Its value is invariant to range misregistrations.

Authorized licensed use limited to: Peking University. Downloaded on March 05,2026 at 17:19:39 UTC from IEEE Xplore. Restrictions apply.

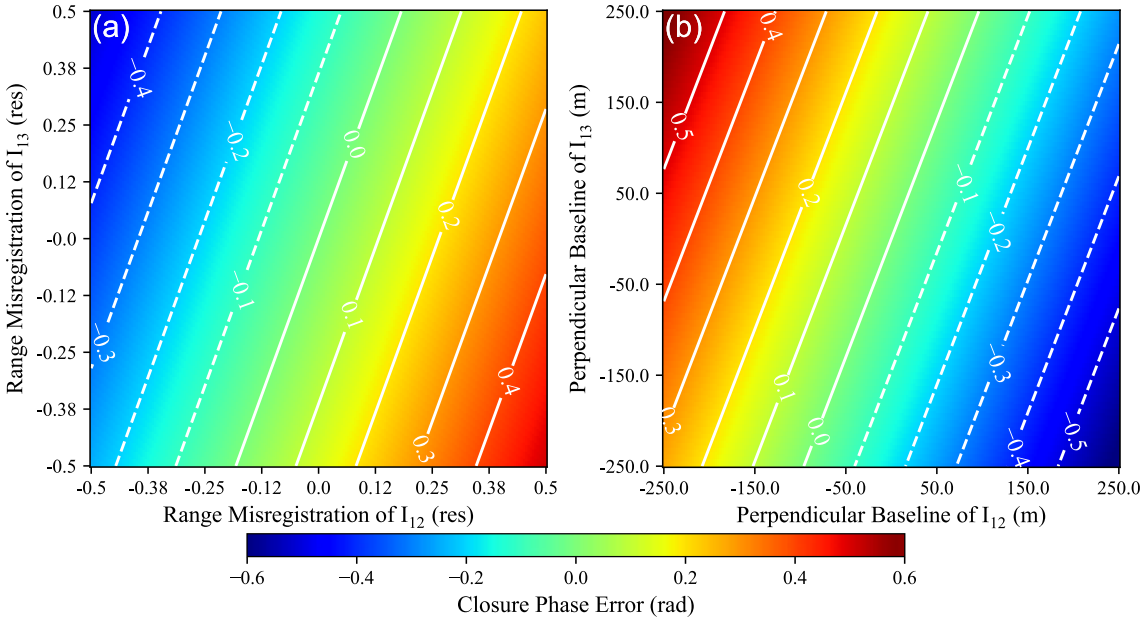


Fig. 7. Closure phase error. (a) Perpendicular baselines are $[b^p_{1,2}, b^p_{1,3}, b^p_{2,3}] = [200, -150, -350]$ m. (b) Range misregistrations are $[r^{\text{mis}}_{1,2}, r^{\text{mis}}_{1,3}, r^{\text{mis}}_{2,3}] = [-0.5, 0.3, 0.8]$ res. The radar center frequency is 1.26 GHz. The range resolution is 10.71 m. The look angle is 35°. The ground slope is 20°.

TABLE I
SIMULATION PARAMETERS FROM SENTINEL-1

| Parameter | Value |
|---|---|
| Center Frequency [GHz] | 5.405 |
| Bandwidth [MHz] | 56.5 |
| Range Sampling Rate [MHz] | 64.3 |
| Pulse Duration [$\mu s$] | 52.4 |
| Look Angle [Deg] | 35 |
| Altitude of the Platform [Km] | 693 |
| Ground Surface Slope [Deg] | 20 |

For a type 2) target, a misregistration $r_{\text{mis}}$ between the reference and secondary images introduces a phase error of

$$\varphi^{\text{distrib}}_{\text{error}} = \frac{4\pi}{c}\Delta f \frac{r_{\text{mis}}}{2} \tag{14}$$

as derived in (8).

For a type 3) target, the phase error can be expressed as a weighted average between the cases of types 1) and 2)

$$\varphi^{\text{domin}}_{\text{error}} = \frac{4\pi}{c}\Delta f \left[\alpha\left(\tilde{r}_{\text{PS}} - r_{0,\text{ref}}\right) + (1-\alpha)\frac{r_{\text{mis}}}{2}\right] \tag{15}$$

where the weighting coefficient $\alpha$ represents the degree to which the target scattering is dominated by the dominant scatterer.

### E. Closure Phase Error Due to Range Misregistration

Nonzero closure phase is a recently identified problem in InSAR [19]. Its impacts on InSAR time series are now widely acknowledged [39]. Previous works have predominantly concentrated on investigating the physical origins of closure phase related to ground surface and subsurface properties [19], [20], [21], [22]. For instance, the closure phase has been proposed as a potential indicator for measuring soil moisture [18], [40], [41]. Here, we identify range misregistration as a factor generating the closure phase.

Consider three SAR images, denoted as $i$, $j$, and $k$, where image $i$ serves as the reference image to which images $j$ and $k$ are coregistered. From this triplet, three interferograms $I_{i,j}$, $I_{j,k}$, and $I_{i,k}$ can be generated. The corresponding range frequency shifts are $\Delta f_{i,j}$, $\Delta f_{j,k}$, and $\Delta f_{i,k}$. Let $r_{0,\text{ref}}$ represent the geometrical center of the reference range resolution cell. The InSAR phase centers of this resolution cell in the three interferograms are denoted as $\tilde{r}_{i,j}$, $\tilde{r}_{j,k}$, and $\tilde{r}_{i,k}$. Following (12), the InSAR phase errors are

$$\begin{cases} \varphi_{i,j} = \dfrac{4\pi}{c}\Delta f_{i,j}\left(\tilde{r}_{i,j} - r_{0,\text{ref}}\right) \\ \varphi_{j,k} = \dfrac{4\pi}{c}\Delta f_{j,k}\left(\tilde{r}_{j,k} - r_{0,\text{ref}}\right) \\ \varphi_{i,k} = \dfrac{4\pi}{c}\Delta f_{i,k}\left(\tilde{r}_{i,k} - r_{0,\text{ref}}\right). \end{cases} \tag{16}$$

The sum of $\Delta f$ satisfies a closure condition

$$\Delta f_{i,j} + \Delta f_{j,k} - \Delta f_{i,k} = 0. \tag{17}$$

Using (17), the closure phase is

$$\begin{aligned} \Delta\varphi_{ijk} &= \varphi_{i,j} + \varphi_{j,k} - \varphi_{i,k} \\ &= \frac{4\pi}{c}\left(\Delta f_{i,j}\tilde{r}_{i,j} + \Delta f_{j,k}\tilde{r}_{j,k} - \Delta f_{i,k}\tilde{r}_{i,k}\right). \end{aligned} \tag{18}$$

Equation (18) shows that the coupling between the range frequency shift and the InSAR phase center violates the closure condition, except in the special case when the InSAR phase centers coincide. Therefore, temporal variations in the InSAR phase center of a resolution cell can generate a nonzero closure phase. These variations primarily originate from two sources: first, differential range misregistrations between the reference and various secondary images, a scenario that is frequently

Authorized licensed use limited to: Peking University. Downloaded on March 05,2026 at 17:19:39 UTC from IEEE Xplore. Restrictions apply.

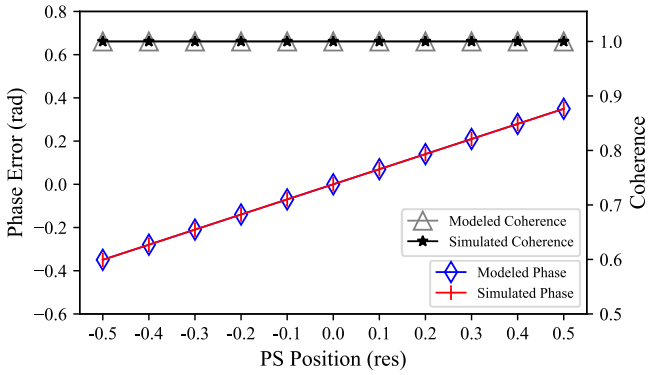


Fig. 8. InSAR phase error of target 1), with the scatterer's position measured from the geometrical center of the resolution cell.

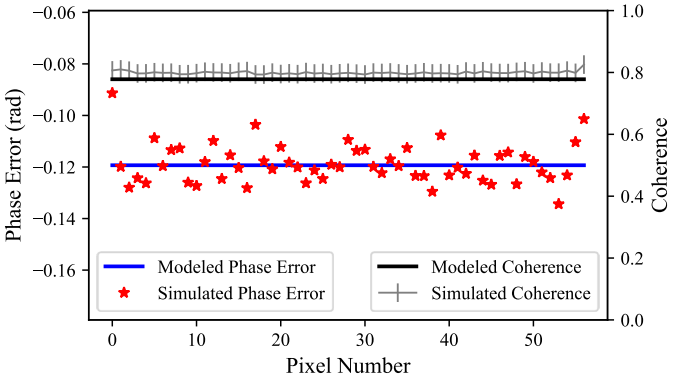


Fig. 9. InSAR phase error and decorrelation of target 2) due to a range misregistration of 0.3 range resolution cell between reference and secondary images.

observed; and second, changes in the inhomogeneity within the resolution cell, e.g., seasonal shifts in the InSAR phase center.

The closure phase, as computed under typical configurations for a triplet with image 1 as the reference, is shown in Fig. 7.

### *F. Corrections of the Phase Errors*

Nevertheless, correcting the InSAR and closure phase errors in (12) and (18) presents a significant challenge. The InSAR phase error is entangled with other phase components in the interferogram. Consequently, it is difficult to isolate based solely on its characteristic signatures. A comparable difficulty arises in the mitigation of closure phase errors.

Alternatively, the errors can be corrected using the expression on the right-hand side of (12), where the InSAR phase error depends on both the range frequency shift $\Delta f = f_0 \Delta\theta / \tan(\theta - \alpha)$ and the range misregistration. A precise calculation of $\Delta f$, however, requires an accurate terrain slope $\alpha$ of the range resolution cell. A rough estimate of the slope can be derived from a publicly available DEM, although the DEM resolution is typically much coarser than that of the SAR image. The primary challenge stems from the general lack of precise range misregistration, as discussed in Section II-B, and knowledge of target types. Given precise range misregistration, a suboptimal correction could be achieved by combining a DEM-derived ground slope with a distributed target assumption. As demonstrated in Section VI, this approach actually proves effective. Therefore, the solution hinges on precisely determining the range misregistration. The range misregistration induced by the ionosphere is mostly smooth, making it easier to obtain a reliable estimate. In contrast, other types of range misregistrations may exhibit significant spatial variability, making their estimation challenging, especially when coherence is low.

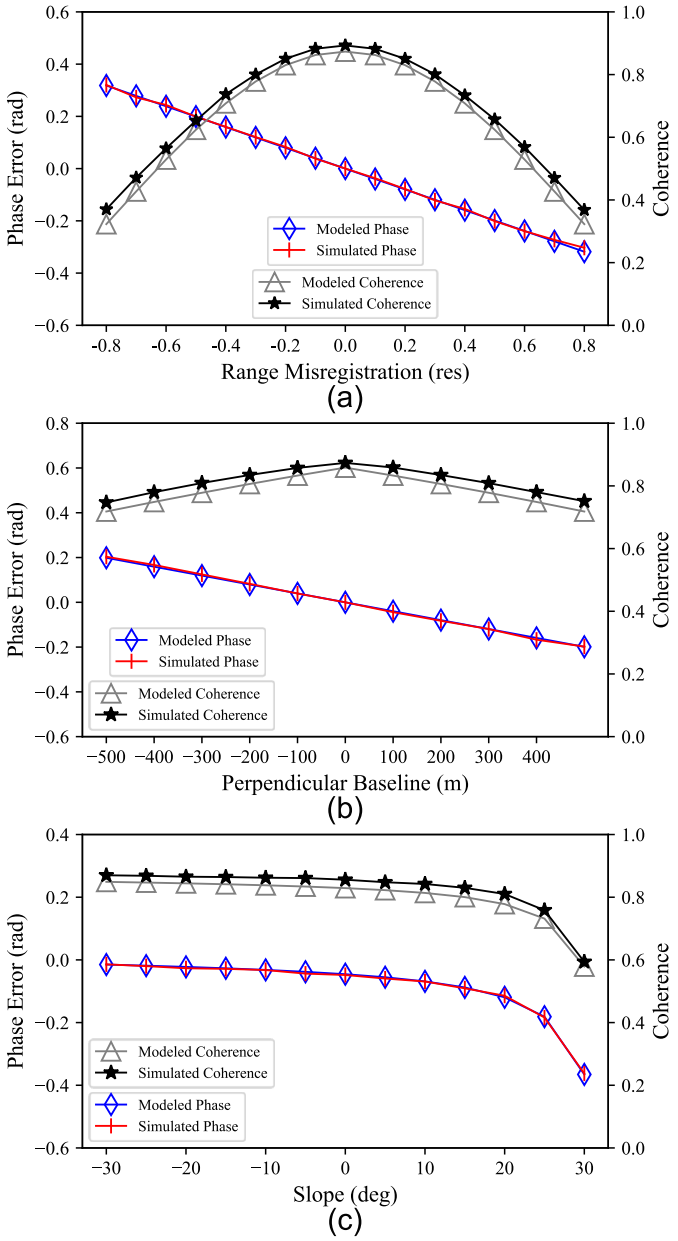


Fig. 10. Sensitivity analysis of InSAR phase error and decorrelation of target 2). Subplots show variations with one parameter while keeping the other two constant. (a) Range misregistration (the perpendicular baseline is 300 m and the ground slope is 20°). (b) Perpendicular baseline (the range misregistration is 0.3 resolution cell and the ground slope is 20°). (c) Ground slope (the range misregistration is 0.3 resolution cell and the perpendicular baseline is 300 m).

### *G. Implications*

As indicated by (12) and (18), both the InSAR and closure phase errors are proportional to the range frequency shift $\Delta f$.

Authorized licensed use limited to: Peking University. Downloaded on March 05,2026 at 17:19:39 UTC from IEEE Xplore. Restrictions apply.

TABLE II
DETAILS OF THE EXPERIMENTAL DATA

| | | | | | |
|---|---|---|---|---|---|
| Sentinel-1 | Western China | Date [YYYY/MM/DD] | 2023/08/10 | 2023/08/22 | 2023/09/03 |
| | | Perp. Baseline [m] | $b^p_{1,2}$ | $b^p_{2,3}$ | $b^p_{1,3}$ |
| | | | 188.2 | 78.5 | 266.7 |
| | Chile-Argentina Border | Date [YYYY/MM/DD] | 2020/10/23 | 2020/11/04 | 2020/11/16 |
| | | Perp. Baseline [m] | $b^p_{1,2}$ | $b^p_{2,3}$ | $b^p_{1,3}$ |
| | | | 126.4 | 27.9 | 154.3 |
| ALOS PALSAR | Chile-Argentina Border | Date [YYYY/MM/DD] | 2008/06/05 | 2009/10/24 | 2010/06/11 |
| | | Perp. Baseline [m] | $b^p_{1,2}$ | $b^p_{2,3}$ | $b^p_{1,3}$ |
| | | | -2120.7 | 1326.0 | -794.7 |
| ALOS-2 PALSAR-2 | Northern Chile | Date [YYYY/MM/DD] | 2017/05/09 | 2017/06/20 | 2020/12/01 |
| | | Perp. Baseline [m] | $b^p_{1,2}$ | $b^p_{2,3}$ | $b^p_{1,3}$ |
| | | | 200.8 | 142.8 | 343.6 |

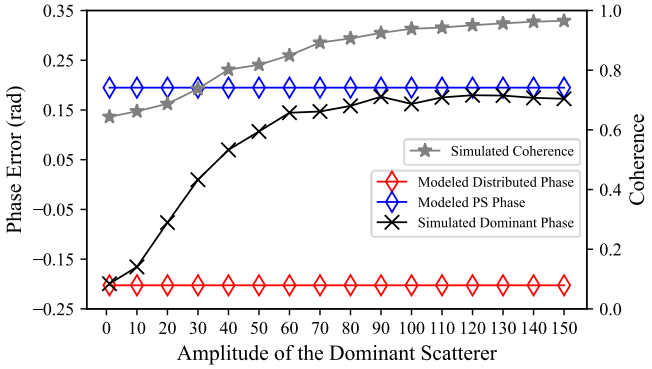


Fig. 11. InSAR phase error and decorrelation of target 3) due to a range misregistration of 0.3 range resolution cell between reference and secondary images.

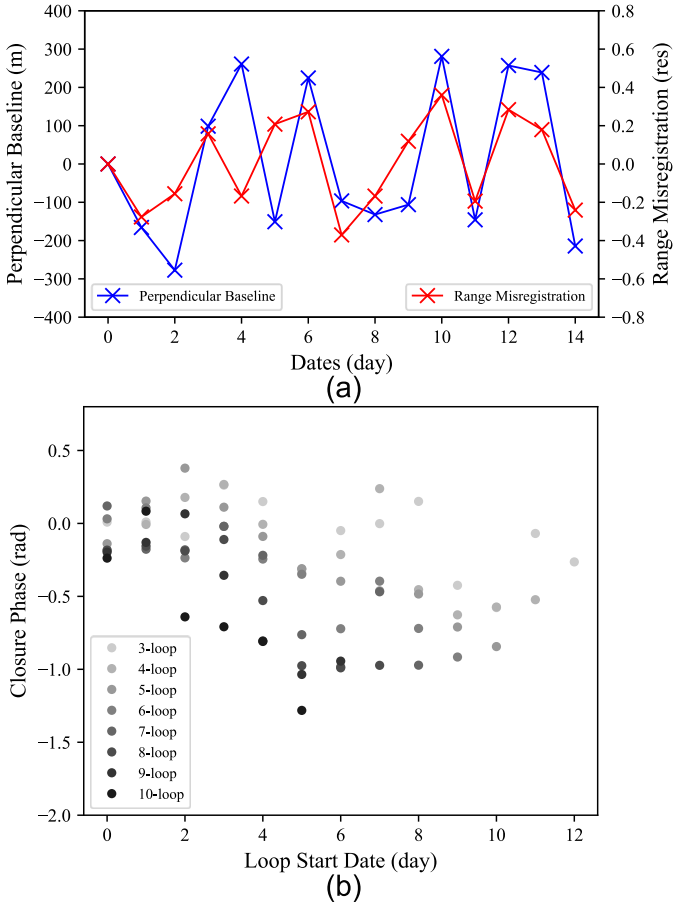


Fig. 12. Nonzero closure phase due to range misregistrations between reference and secondary images. (a) Perpendicular baselines and range misregistrations between reference and secondary images. (b) Closure phases of sequential loops.

Minimizing these errors necessitates the use of a small orbit tube, a requirement that is also consistent with other considerations in InSAR theories. Since $\Delta f$ is a function of local ground slope, the resulting InSAR and closure phase errors should exhibit correlations with topography. This correlation suggests that some topographic-correlated anomalies observed in InSAR and closure phase can be attributed to these errors. Notably, despite the small orbit tubes in current representative satellites, local $\Delta f$ values might still be significant due to their dependence on ground slope.

The InSAR and closure phase errors also depend on range misregistrations. Achieving high-precision range coregistration, however, is inherently challenging, as discussed in Section II. In fact, this issue has received considerably less attention compared to azimuth coregistration. The InSAR and closure phase errors induced by range misregistration argue for its necessity and highlight that it demands careful handling.

The InSAR phase error is generally negligible compared to other dominant phase components in a single interferogram and therefore has minimal impact on applications relying on individual InSAR pairs. In contrast, the closure phase error is significant as the closure phase itself is typically a small quantity. This is particularly critical for time series analysis, where the error can introduce a systematic bias. For instance, in mountainous regions, it may manifest as a velocity difference between the slopes facing toward and away

Authorized licensed use limited to: Peking University. Downloaded on March 05,2026 at 17:19:39 UTC from IEEE Xplore. Restrictions apply.

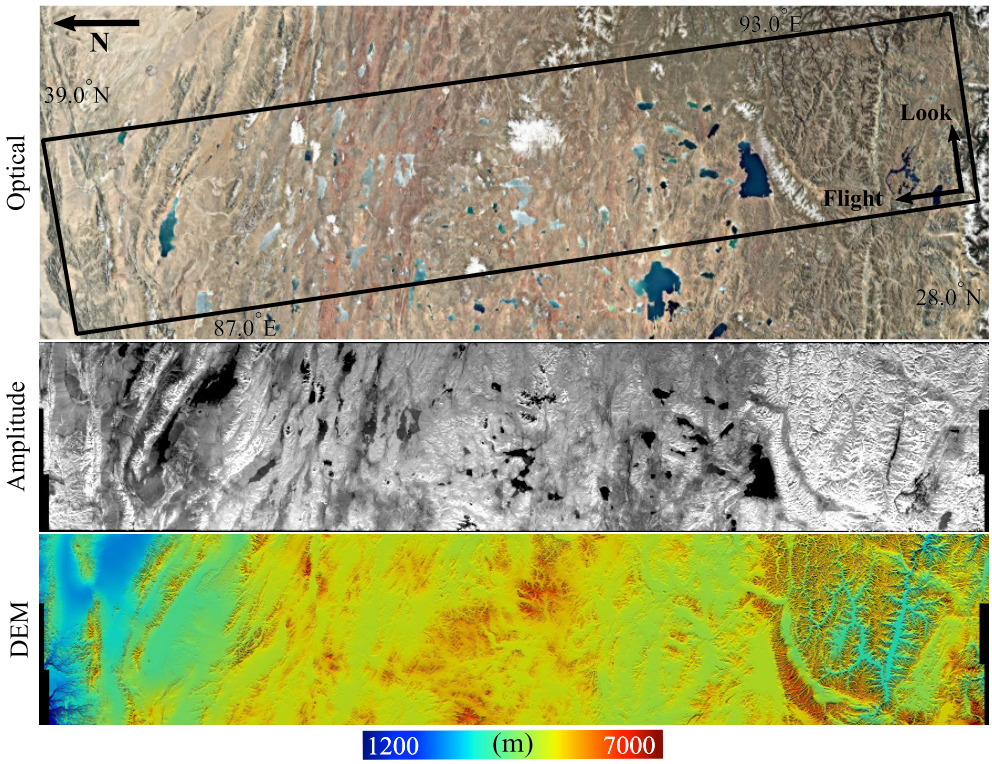


Fig. 13. Optical image, SAR amplitude image, and DEM of the study area located in western China.

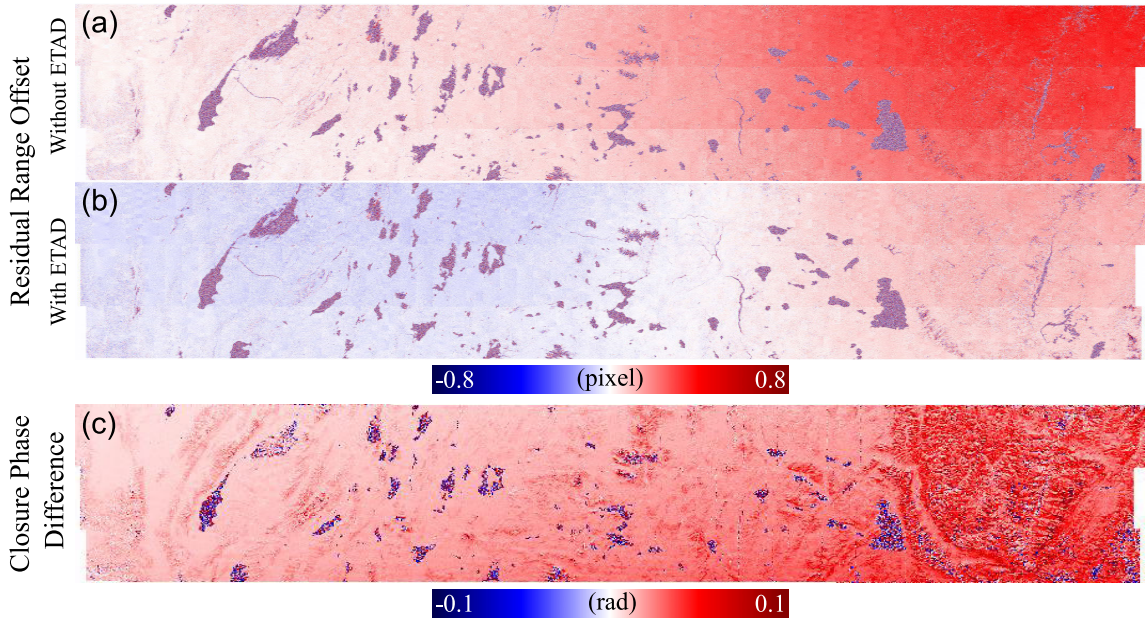


Fig. 14. Residual range offsets estimated using the cross correlation method after geometrical coregistration (a) without and (b) with corrections from the ETAD product for the InSAR pair 2023/08/10–2023/08/22. (c) Difference between closure phases with and without ETAD corrections. These results are derived from Sentinel-1 data acquired over western China.

from the radar, thereby compromising the accuracy of InSAR time series measurements in such terrain. It is also necessary to consider these errors in physical measurements based on the closure phase, such as soil moisture retrieval. Although such measurements are typically conducted over relatively flat terrain, it remains necessary to account for closure phase errors due to range misregistrations. This is because range misregistrations can exhibit spatial variations, as exemplified in Fig. 2.

## V. Simulation

This section validates the proposed theory through simulations.

### A. InSAR Phase Error

In our simulations, scatterers are arranged along a uniformly sloped, smooth surface, as shown in Fig. 4. Their distribution and reflectivity are defined by the target type established in Section IV-D: target 1) consists of a single scatterer; target 2)

Authorized licensed use limited to: Peking University. Downloaded on March 05,2026 at 17:19:39 UTC from IEEE Xplore. Restrictions apply.

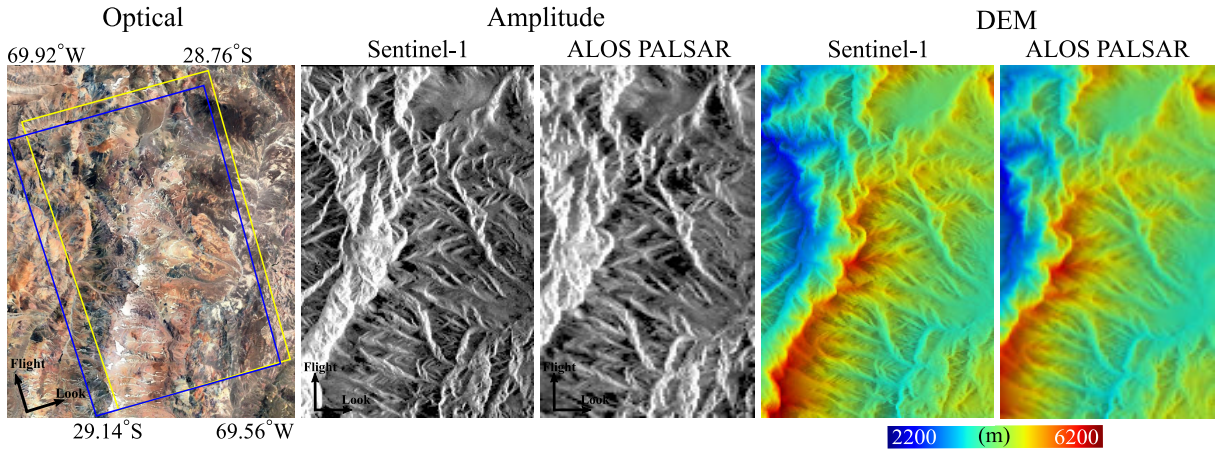


Fig. 15. Optical image, SAR amplitude image, and DEM of the study area across the Chile–Argentina border. The blue and yellow boxes in the optical image outline the coverage of Sentinel-1 and ALOS PALSAR images, respectively.

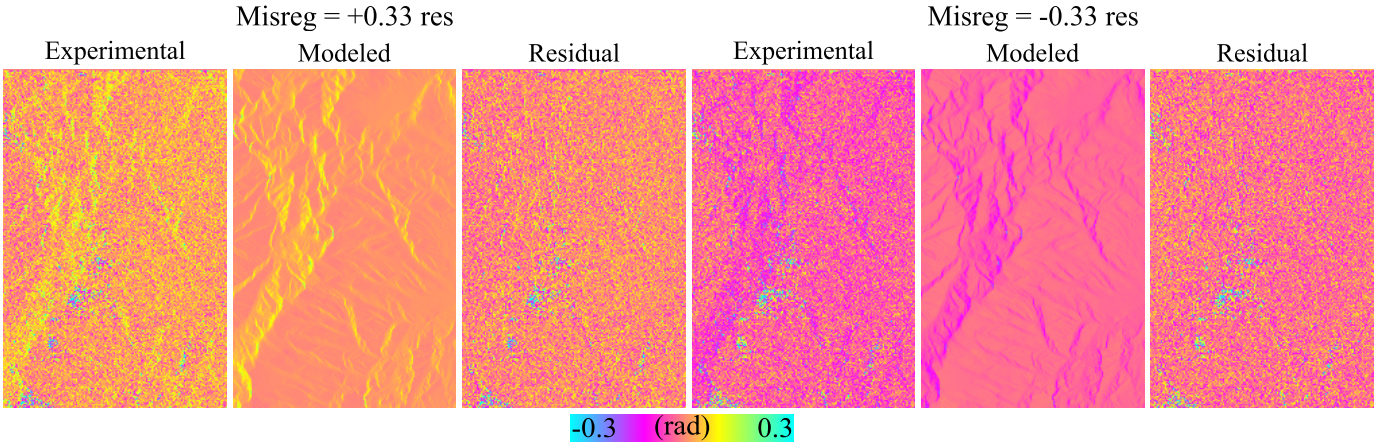


Fig. 16. Experimental versus modeled InSAR phase errors due to range misregistrations, derived from Sentinel-1 data across the Chile–Argentina border. The InSAR pair used here is 2020/10/23–2020/11/04.

is distributed spanning 57 range pixels; and target 3) is derived from target 2) by introducing an additional dominant scatterer with a relatively higher reflectivity.

Our simulation implements the complete SAR processing workflow, from raw data acquisition to interferogram formation, using Sentinel-1 system parameters in Table I. The process begins with generating a linear frequency-modulated (FM) signal. The raw radar echoes are then simulated by convolving this signal with the ground reflectivity. The raw data are focused using matched filtering to produce two SAR images. These images, designated as reference and secondary, are generated with the antenna phase centers separated by a defined spatial baseline. The range offset between the reference and secondary image can be accurately determined based on the imaging geometry, thereby enabling a precise coregistration. For targets 2) and 3), the secondary image is additionally resampled with an introduced range offset error to simulate the range misregistration effects. Subsequently, the interferogram is generated with the topographic phase component removed at the geometrical center of the resolution cell. Unless otherwise specified, the simulations are repeated 500 times to estimate the expected values of both the InSAR phase and coherence.

For target 1), the scatterer is positioned at various locations within the range resolution cell, while the perpendicular baseline is held constant at 100 m. The results are presented in Fig. 8. The theoretical phase error, calculated using (13), demonstrates that the InSAR phase error is dependent on the scatterer's position relative to the geometrical center of the resolution cell. As expected, the degree of decorrelation remains relatively low throughout.

For target 2), a scenario comprising 57 pixels, each containing 300 scatterers, is simulated. A range misregistration of 0.3 range resolution cell is introduced between the reference and secondary images, while the perpendicular baseline is still 100 m. The simulation is executed over 5000 times to estimate the expected phase error and coherence. The results, presented in Fig. 9, show that the phase error is accurately predicted by the model in (14). The simulated coherence, however, is slightly higher than the theoretical value derived from (11). This discrepancy arises because the theoretical model assumes an infinite number of scatterers contributing to the SAR signal, whereas the practical simulation is constrained by a finite number of effective scatterers, limited by the pulse and matched filter lengths.

Authorized licensed use limited to: Peking University. Downloaded on March 05,2026 at 17:19:39 UTC from IEEE Xplore. Restrictions apply.

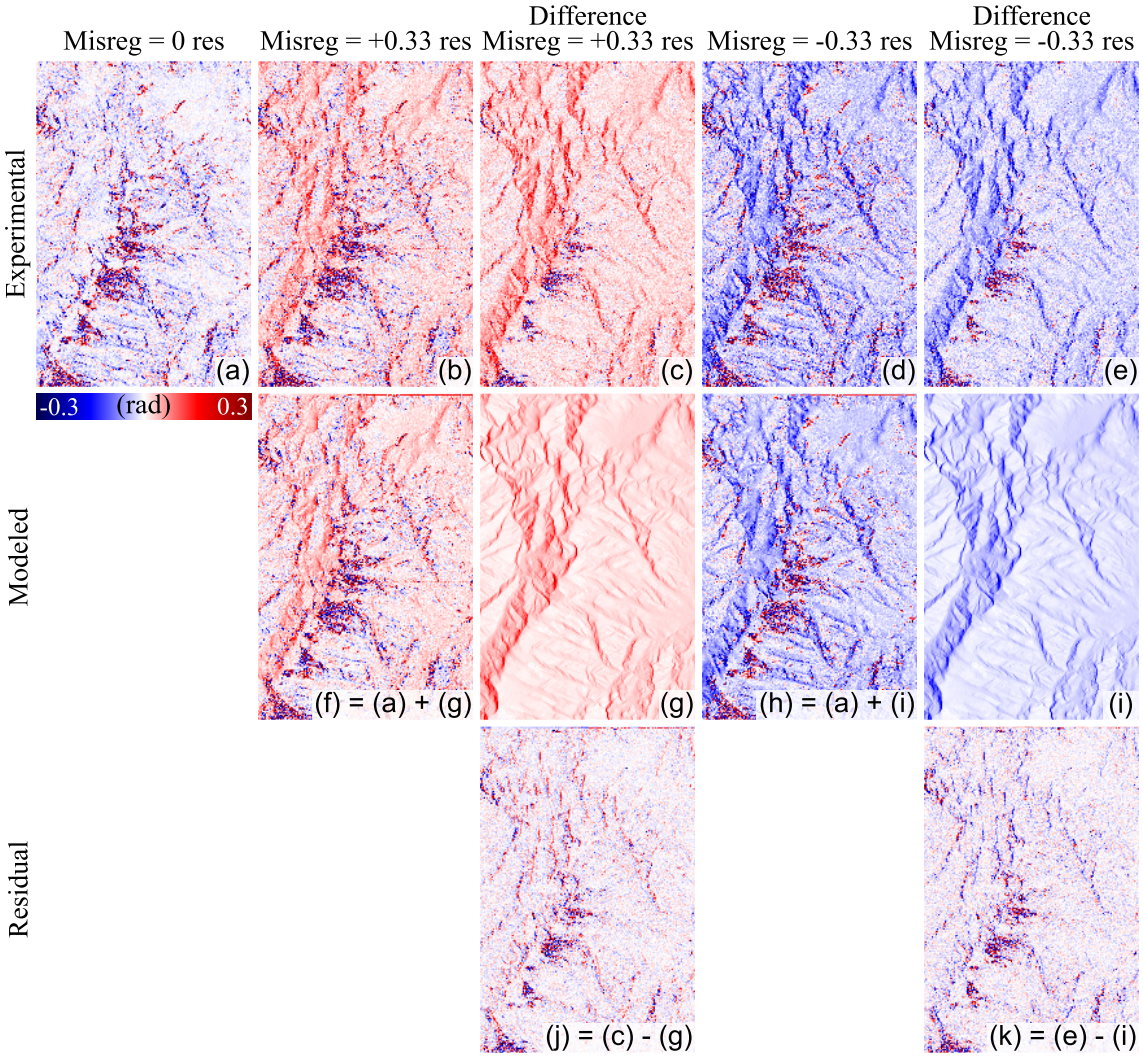


Fig. 17. Experimental versus modeled closure phase errors due to range misregistrations, derived from Sentinel-1 data across the Chile–Argentina border. The range misregistrations are added for the image acquired on 2020/11/04. (a) Original closure phase. (b) Experimental closure phase with a range misregistration of +0.33 range resolution cell. (c) Closure phase difference between (a) and (b). (d) Experimental closure phase with a range misregistration of -0.33 range resolution cell. (e) Closure phase difference between (a) and (d). (f) Modeled closure phase with a range misregistration of +0.33 range resolution, derived from (a)+(g). (g) Modeled closure phase error with a range misregistration of +0.33 range resolution cell. (h) Modeled closure phase with a range misregistration of -0.33 range resolution, derived from (a)+(i). (i) Modeled closure phase error with a range misregistration of -0.33 range resolution cell. (j) Residual closure phase error between the experimental and modeled results with a range misregistration of +0.33 range resolution cell, obtained as (c)-(g). (k) Residual closure phase error between the experimental and modeled results with a range misregistration of -0.33 range resolution cell, obtained as (e)-(i).

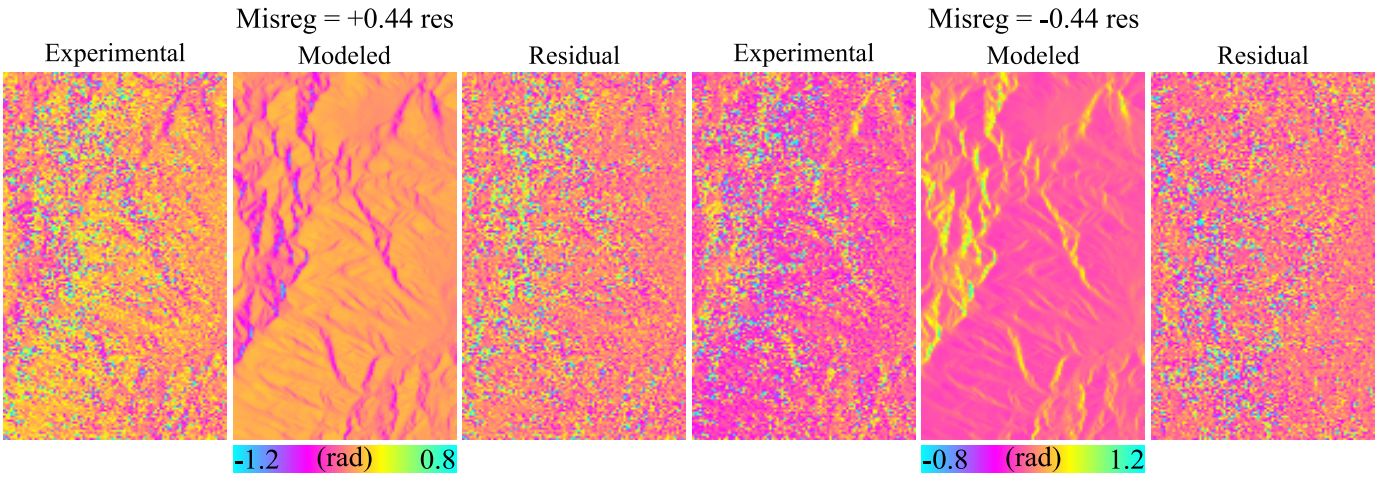


Fig. 18. Experimental versus modeled InSAR phase errors due to range misregistrations, derived from ALOS PALSAR data across the Chile–Argentina border. The InSAR pair used here is 2008/06/05–2009/10/24.

Authorized licensed use limited to: Peking University. Downloaded on March 05,2026 at 17:19:39 UTC from IEEE Xplore. Restrictions apply.

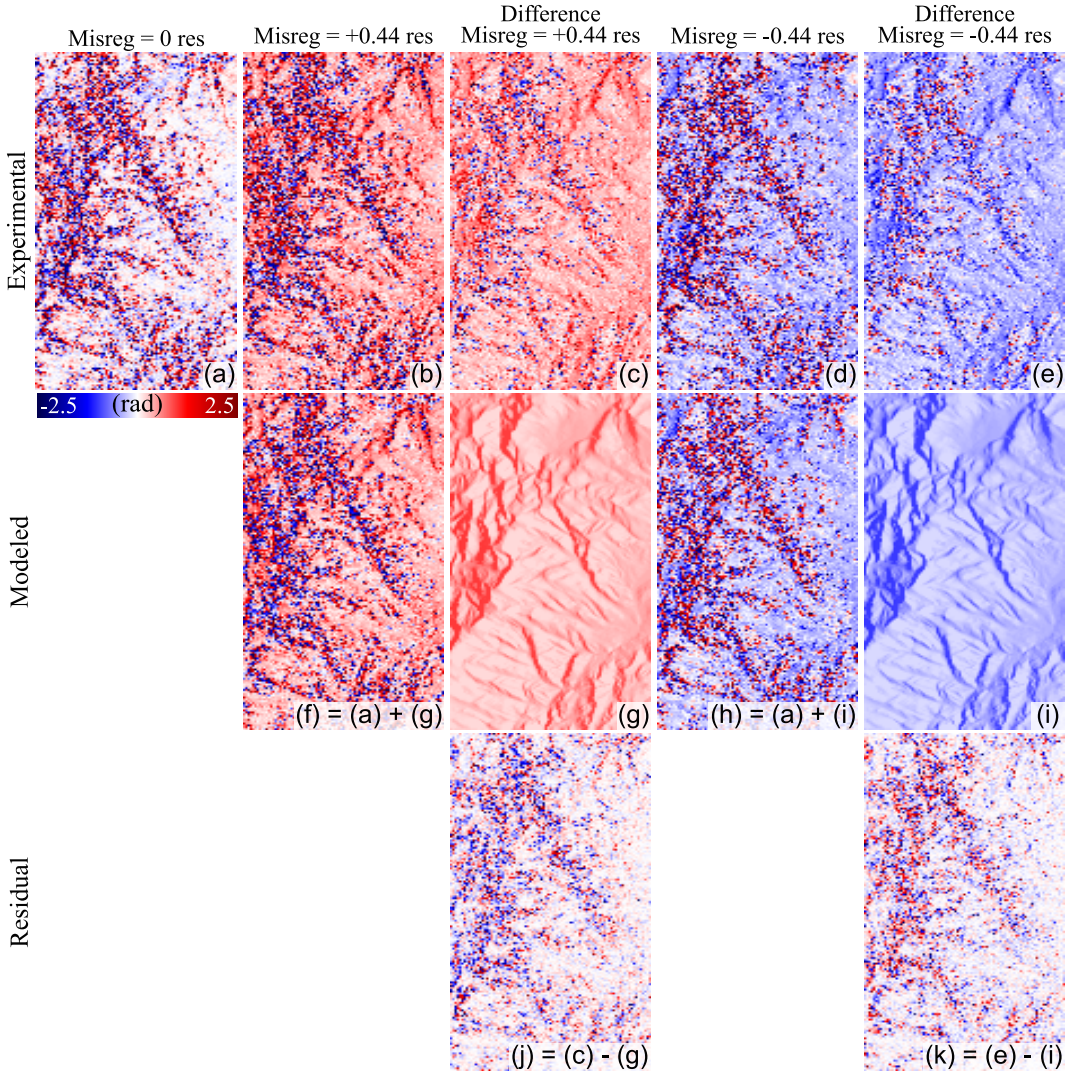


Fig. 19. Experimental versus modeled closure phase errors due to range misregistrations, derived from ALOS PALSAR data across the Chile–Argentina border the range misregistrations are added for the image acquired on 2010/06/11. (a) Original closure phase. (b) Experimental closure phase with a range misregistration of +0.44 range resolution cell. (c) Closure phase difference between (a) and (b). (d) Experimental closure phase with a range misregistration of -0.44 range resolution cell. (e) Closure phase difference between (a) and (d). (f) Modeled closure phase with a range misregistration of +0.44 range resolution, derived from (a)+(g). (g) Modeled closure phase error with a range misregistration of +0.44 range resolution cell. (h) Modeled closure phase with a range misregistration of -0.44 range resolution, derived from (a)+(i). (i) Modeled closure phase error with a range misregistration of -0.44 range resolution cell. (j) Residual closure phase error between the experimental and modeled results with a range misregistration of +0.44 range resolution cell, obtained as (c)-(g). (k) Residual closure phase error between the experimental and modeled results with a range misregistration of -0.44 range resolution cell, obtained as (e)-(i).

The InSAR phase error and decorrelation vary as a function of range misregistration, perpendicular baseline, and ground slope, as illustrated by the simulation results in Fig. 10.

For target 3), the dominant scatterer is positioned 0.26 resolution cell from the geometrical center of the resolution cell. The RCS ratio of this dominant scatterer to the others is swept from 1 to a substantially high value, under a constant range misregistration of 0.3 resolution cell. The results, presented in Fig. 11, show that as the RCS ratio increases, the phase error transitions from the behavior characteristic of target 2) to that of target 1), a trend well-explained by (15). As expected, this transition is accompanied by a systematic reduction in coherence.

### B. Closure Phase Error

To analyze the closure phase error, we generate an image stack for a distributed target by following the method outlined in Section V-A. The stack consists of 15 SAR images, with the first image designated as the reference. The perpendicular baselines between the reference and secondary images are randomly distributed within the range of −300 to 300 m. The secondary images are coregistered to the reference image with random range misregistrations varying between −0.4 and 0.4 resolution cell. The closure phases are then computed for sequential loops, where an N-acquisition sequential loop is defined as a sequence of N consecutively acquired images. The parameter N is varied from 3 to 10, with different starting dates considered for each loop. The results, presented in Fig. 12, exhibit significant nonzero closure phases.

## VI. Real-Data Experiment

This section validates the theoretical models for InSAR and closure phase errors induced by range misregistrations between reference and secondary SAR images through experiments on real SAR datasets. The data used include C-band Sentinel-1 TOPS mode, L-band ALOS PALSAR FBD mode, and

Authorized licensed use limited to: Peking University. Downloaded on March 05,2026 at 17:19:39 UTC from IEEE Xplore. Restrictions apply.

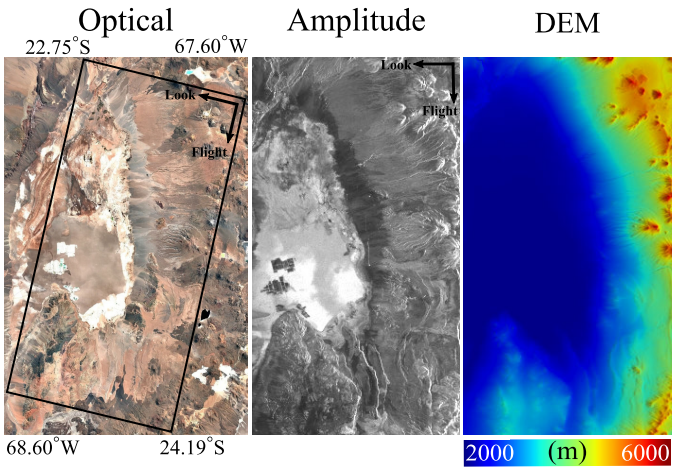


Fig. 20. Optical image, SAR amplitude image, and DEM of the study area in northern Chile.

ALOS-2 PALSAR-2 ScanSAR mode acquisitions, with key parameters summarized in Table II. Each dataset, comprising three images, is processed using topsStack [42], alosStack [28], and stripmapApp [43] in the ISCE software packages. The first acquisition in each stack is designated as the reference image, with the subsequent two images coregistered to it. For the Sentinel-1 dataset acquired over western China, we compare the closure phases generated using range geometrical offsets with and without corrections from the Extended Timing Annotation Dataset (ETAD) product [44]. For the other datasets, the InSAR and closure phase errors caused by introduced range misregistrations are compared with the theoretical predictions derived from (14), thereby validating the correction method proposed in Section IV-F.

### A. C-Band Sentinel-1

Fig. 13 presents the optical image, SAR amplitude image, and DEM of a study area located in western China. The dataset was acquired by Sentinel-1 in TOPS mode. As shown in Fig. 14(a), a spatially varying residual range offset, estimated using the cross correlation method, persists after geometrical coregistration. The residual range offset is primarily attributed to ionospheric delay, and the ETAD product is employed to correct the geometrical range offset. A comparison of the closure phases with and without ETAD corrections reveals a notable difference, as shown in Fig. 14(c).

Fig. 15 presents the optical image, SAR amplitude image, and DEM of a study area across the Chile–Argentina border. This experiment uses data from swath three of Sentinel-1 TOPS mode, which has a range resolution of 3.50 m. We introduce range misregistrations of $\pm 0.33$ range resolution cell ($\pm 1.16$ m) to the range geometrical offset for the image acquired on 2020/11/04. It is important to note that in real scenarios, such range misregistration is not a constant but exhibits spatial variability, as illustrated in Figs. 1, 2, and 14.

Figs. 16 and 17 present a comparison between the experimental results and the modeled predictions for both the InSAR and closure phase errors due to range misregistrations. The close agreement between the observations and the theoretical values calculated from (14) demonstrates the model's validity. These errors exhibit a clear topographic dependence. The residuals are primarily random noise, though they show a correlation with topography in rugged areas due to errors in the DEM.

The closure phase errors presented in Fig. 17 are of a magnitude that cannot be disregarded. They would bias the physical measurements using closure phase and adversely impact the quality of InSAR time series results [39].

### B. L-Band ALOS PALSAR

The ALOS PALSAR data used in this experiment cover a region nearly identical to that of the Sentinel-1 study area in Fig. 15. With a range resolution of 10.71 m, range misregistrations of $\pm 0.44$ range resolution cell ($\pm 4.68$ m) are intentionally introduced to the range geometrical offset of the image acquired on 2010/06/11.

Figs. 18 and 19 present the experimental and modeled results of InSAR and closure phase errors due to range misregistrations. Once again, the model from (14) accurately captures the observed errors. Due to the poorly constrained ALOS baselines, which are notably larger, the resulting InSAR and closure phase errors are substantially greater than those from Sentinel-1. This contrast highlights the fundamental necessity of baseline control in InSAR applications, as also required by other InSAR theories.

### C. L-Band ALOS-2 PALSAR-2

Fig. 20 shows the optical image, SAR amplitude image, and DEM for a study area in northern Chile, imaged by ALOS-2 PALSAR-2 in ScanSAR mode, with a range resolution of 12.60 m. Range misregistrations of $\pm 0.34$ and $\pm 0.68$ range resolution cell ($\pm 4.29$ and $\pm 8.58$ m) are intentionally imposed on the cross correlation-estimated range offset for the data acquired on 2017/06/20. Furthermore, the images are segmented into four equal parts, with each quadrant assigned a different misregistration value to demonstrate the impact of its spatial variations.

Figs. 21 and 22 present a comparison between the experimental measurements and the model predictions for the InSAR and closure phase errors induced by the applied range misregistrations. As in the previous cases, (14) effectively models the observed errors. In contrast to the first two experiments, the topography of this area is predominantly flat. Consequently, the phase errors do not exhibit the pronounced spatial variations observed in the previous, more rugged terrains.

Fig. 23 illustrates the closure phase errors from the spatially varying range misregistrations applied in this experiment. In practical scenarios, the spatial patterns of range misregistrations may be smooth, which makes their contributions difficult to isolate from other contributions.

## VII. Conclusion

This article has systematically analyzed the phase errors in InSAR measurements due to the range misregistrations between the reference SAR image and DEM, and between the reference and secondary images, as well as the inhomogeneity within the range resolution cell. We find that all these can

Authorized licensed use limited to: Peking University. Downloaded on March 05,2026 at 17:19:39 UTC from IEEE Xplore. Restrictions apply.

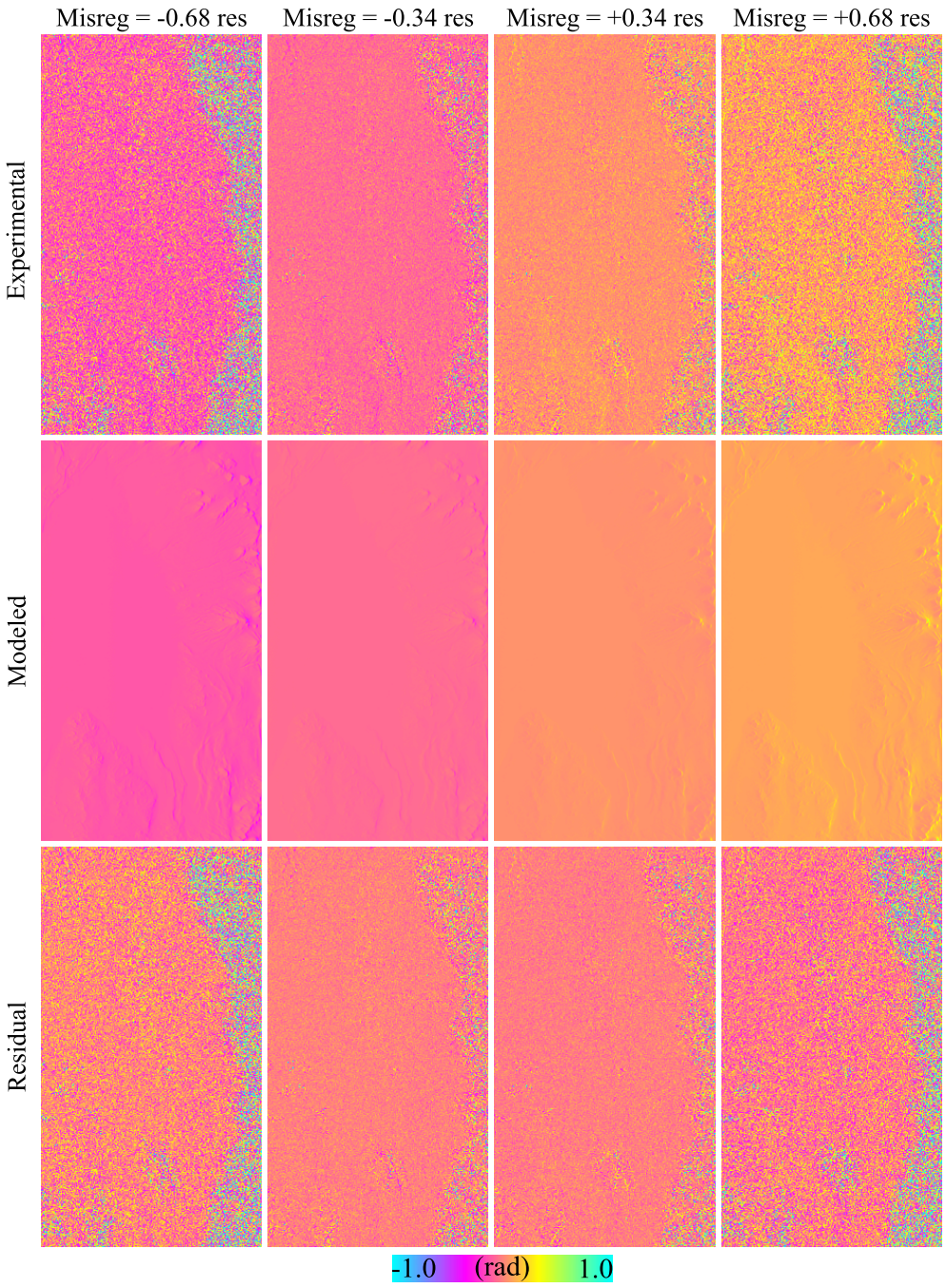


Fig. 21. Experimental versus modeled InSAR phase errors due to range misregistrations, derived from ALOS-2 PALSAR-2 data of the study area in northern Chile. The InSAR pair used here is 2017/05/09–2017/06/20.

be fundamentally attributed to a misregistration between the reference image and DEM, which manifests directly as an InSAR phase error. Moreover, we demonstrate that a closure phase error can be induced by the InSAR phase errors from the range misregistration between the reference and secondary images, as well as the inhomogeneity of the range resolution cell. These effects should be considered in any application depending on phase consistency, including closure phase-based physical measurements (such as soil moisture estimation) and time series analysis techniques.

The phase error due to range misregistration is proportional to both the range offset error and the perpendicular baseline. This relationship highlights the importance of precise range coregistrations, a factor that has often been underestimated. Furthermore, it emphasizes the necessity of a tightly controlled orbit tube, which is also supported by other foundational principles of InSAR.

## APPENDIX

Here, we derive the InSAR phase error from a signal theory perspective. Under the first-order Born approximation, the SAR range resolution cell is modeled as comprising numerous independent homogeneous elementary scatterers. The total reflectivity of the resolution cell is thus the superposition of the individual reflectivities of these elementary scatterers.

Authorized licensed use limited to: Peking University. Downloaded on March 05,2026 at 17:19:39 UTC from IEEE Xplore. Restrictions apply.

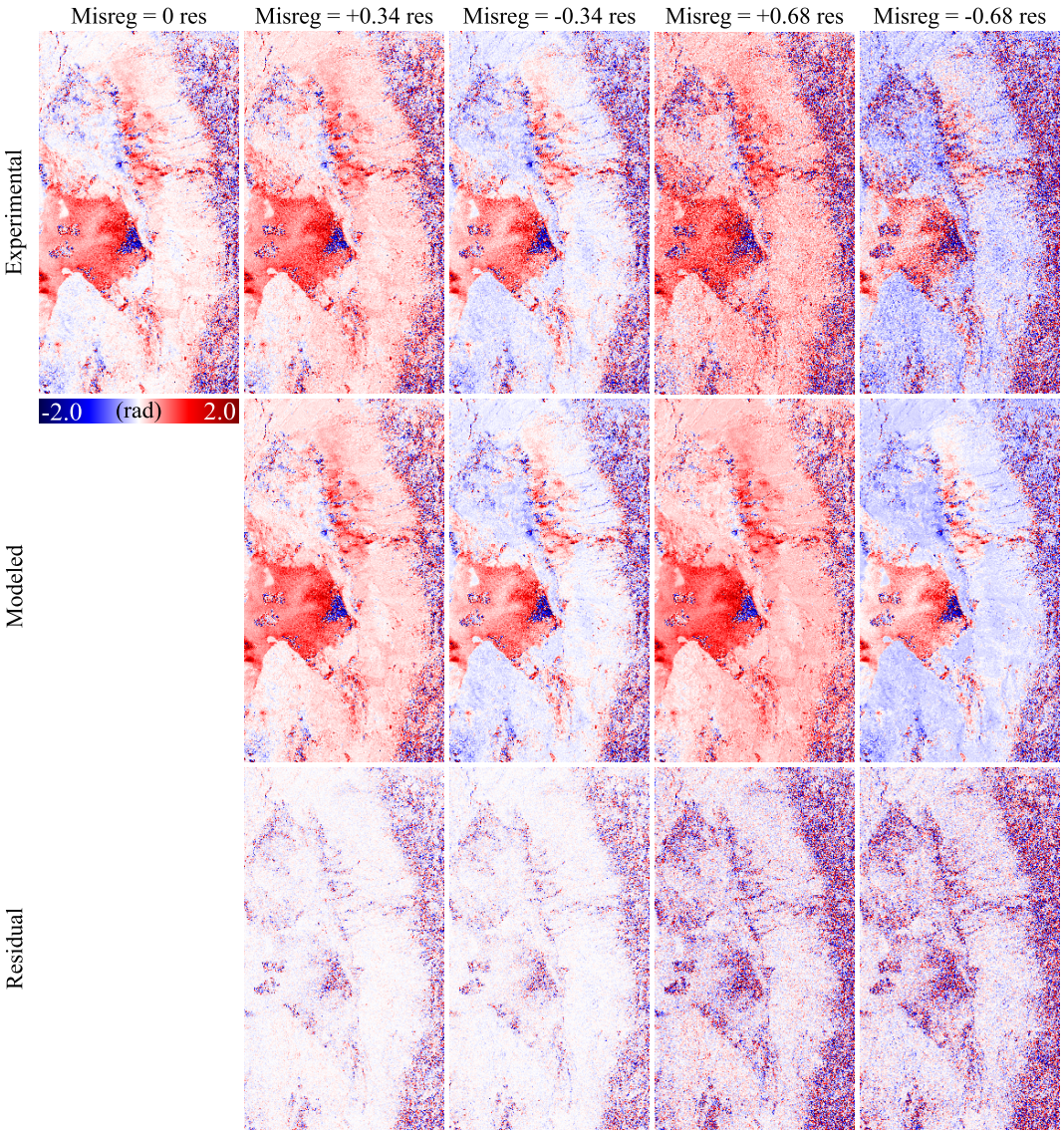


Fig. 22. Experimental versus modeled closure phase errors due to range misregistrations, derived from ALOS-2 PALSAR-2 data of the study area in northern Chile.

In range, the focused SAR image can be represented as the convolution of the ground's complex reflectivity with the SAR impulse response function (IRF)

$$S_{\text{ref}}(t_{\text{ref}}) = \sum_{i=1}^{N} s_i\left(t_{0,\text{ref}} + u_{i,\text{ref}}\right) \operatorname{sinc}\left[KT\left(t_{\text{ref}} - t_{0,\text{ref}} - u_{i,\text{ref}}\right)\right] \exp\left\{-j2\pi f_0\left(t_{0,\text{ref}} + u_{i,\text{ref}}\right)\right\} \tag{19}$$

where $t_{\text{ref}}$ is the reference range time coordinate system, $t_{0,\text{ref}}$ is the reference range time at the geometrical center of the resolution cell (e.g., point $O$ in Fig. 4), $N$ is the number of scatterers in a resolution cell, $s_i(\cdot)$ is the complex reflectivity of scatterer $i$, $\operatorname{sinc}(\cdot)$ is the range IRF, $K$ is the range chirp rate, $T$ is the range chirp duration, and $u_{i,\text{ref}}$ is the relative time delay between scatterer $i$ and the geometrical center in the reference geometry. The total time delay of scatterer $i$ in the reference geometry is $t_{0,\text{ref}} + u_{i,\text{ref}}$. This is the reference image.

Similarly, the secondary image is

$$\begin{aligned} S_{\text{sec}}(t_{\text{sec}}) &= \sum_{i=1}^{N} s_i\left(t_{0,\text{sec}} + u_{i,\text{sec}}\right) \operatorname{sinc}\left[KT\left(t_{\text{sec}} - t_{0,\text{sec}} - u_{i,\text{sec}}\right)\right] \exp\left\{-j2\pi f_0\left(t_{0,\text{sec}} + u_{i,\text{sec}}\right)\right\} \\ &= \sum_{i=1}^{N} s_i\left(t_{0,\text{ref}} - t_b + u_{i,\text{sec}}\right) \operatorname{sinc}\left[KT\left(t_{\text{sec}} - t_{0,\text{ref}} + t_b - u_{i,\text{sec}}\right)\right] \exp\left\{-j2\pi f_0\left(t_{0,\text{ref}} - t_b + u_{i,\text{sec}}\right)\right\} \end{aligned} \tag{20}$$

where $t_{\text{sec}}$ is the secondary range time coordinate system, $t_{0,\text{sec}} = t_{0,\text{ref}} - t_b$ is the secondary range time at the geometrical center of the resolution cell, and $t_b = 2b_r/c$.

Following coregistration of the secondary image to the reference image for interferometry, the secondary image is aligned with the range time coordinate system of the reference image. As a result, both images share a common time variable

Authorized licensed use limited to: Peking University. Downloaded on March 05,2026 at 17:19:39 UTC from IEEE Xplore. Restrictions apply.

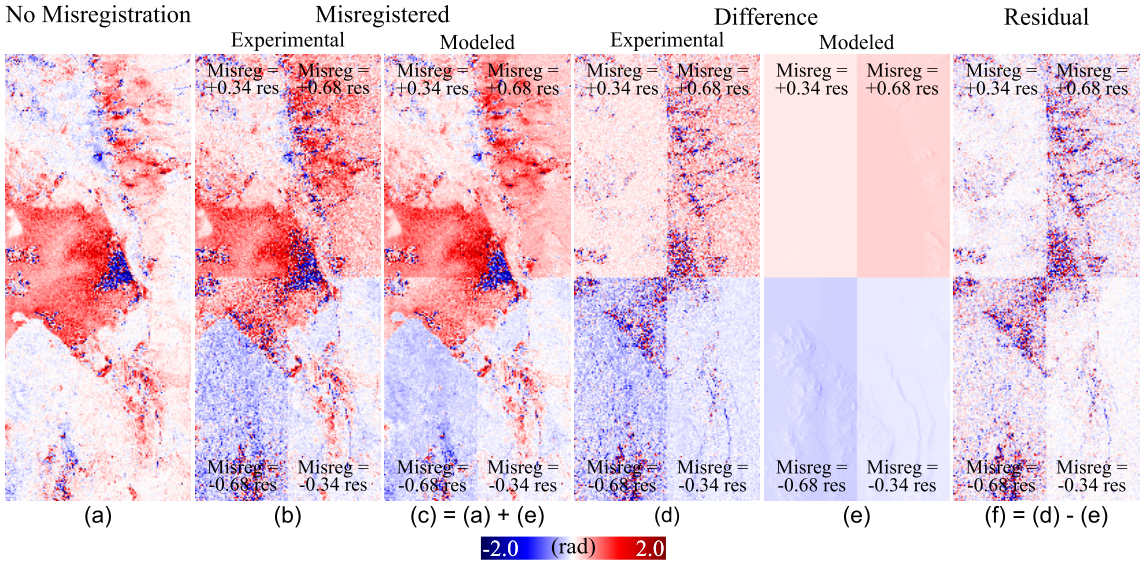


Fig. 23. Experimental versus modeled closure phase errors due to spatially varying range misregistrations, derived from ALOS-2 PALSAR-2 data of the study area in northern Chile. The range misregistrations are added for the image acquired on 2017/06/20. (a) Original closure phase. (b) Experimental closure phase with spatially varying range misregistrations. (c) Modeled closure phase with spatially varying range misregistrations, derived from (a)+(e). (d) Closure phase difference between (a) and (b). (e) Modeled closure phase error with spatially varying range misregistrations. (f) Residual closure phase error between the experimental and modeled results with spatially varying range misregistrations.

in their sinc(·) functions. Accordingly, the interferogram $I(\cdot)$ is defined within this coordinate system, as indicated by the variable $t_{\text{ref}}$. Let $t_{\text{ref}} = t_{0,\text{ref}}$, and the expected value of the interferogram at the geometrical center of the resolution cell is

$$\begin{aligned} & I\left(t_{0,\text{ref}}\right) \\ & = E\left(S_{\text{ref}} S_{\text{sec}}^{*}\right) | t_{\text{ref}} = t_{0,\text{ref}} \\ & = \sum_{i=1}^{N} E\left(|s_i|^2\right) \operatorname{sinc}\left[KT\left(t_{\text{ref}} - t_{0,\text{ref}} - u_{i,\text{ref}}\right)\right] \\ & \qquad \operatorname{sinc}\left[KT\left(t_{\text{ref}} - t_{0,\text{ref}} - u_{i,\text{ref}}\right)\right] \\ & \qquad \exp\left\{j2\pi f_0\left(-t_b + u_{i,\text{sec}} - u_{i,\text{ref}}\right)\right\} | t_{\text{ref}} = t_{0,\text{ref}} \\ & = \sum_{i=1}^{N} E\left(|s_i|^2\right) \operatorname{sinc}\left(-KTu_{i,\text{ref}}\right) \\ & \qquad \operatorname{sinc}\left(-KTu_{i,\text{ref}}\right) \\ & \qquad \exp\left\{j2\pi f_0\left(-t_b + u_{i,\text{sec}} - u_{i,\text{ref}}\right)\right\} \end{aligned} \tag{21}$$

where $|s_i|^2 = \sigma_i$ is the RCS of scatterer $i$ (neglecting $4\pi$) in the far field [38]. In addition, the cross-product terms between different scatterers have canceled out, leaving only the self-interaction terms from individual scatterers in the second line of (21). Following the relationship in (2)

$$u_{i,\text{ref}} - u_{i,\text{sec}} = -\frac{\Delta\theta}{\tan(\theta - \alpha)} u_{i,\text{ref}} \tag{22}$$

the interferogram is

$$I\left(t_{0,\text{ref}}\right) = \sum_{i=1}^{N} E\left(|s_i|^2\right) \operatorname{sinc}\left(-KTu_{i,\text{ref}}\right) \operatorname{sinc}\left(-KTu_{i,\text{ref}}\right) \exp\left\{j2\pi\left(-f_0 t_b + \Delta f u_{i,\text{ref}}\right)\right\}. \tag{23}$$

Assume that the elementary scatterers' reflectivities are independent, zero-mean, circularly symmetric complex Gaussian random variables with a variance of $\sigma/2$ [17]

$$\text{pdf}\left(s_i\right) = \frac{1}{\pi\sigma} \exp\left\{-\frac{|s_i|^2}{\sigma}\right\}. \tag{24}$$

The RCS of each scatterer has an expected value of

$$E\left(|s_i|^2\right) = \sigma. \tag{25}$$

Furthermore, if the range misregistration between the reference and secondary images is $t_{\text{mis}}$, then the interferogram becomes

$$\begin{aligned} I\left(t_{0,\text{ref}}\right) = \sigma \sum_{i=1}^{N} & \operatorname{sinc}\left(-KTu_{i,\text{ref}}\right) \\ & \operatorname{sinc}\left[KT\left(-u_{i,\text{ref}} + t_{\text{mis}}\right)\right] \\ & \exp\left\{j2\pi\left[-f_0 t_b + \Delta f u_{i,\text{ref}}\right]\right\}. \end{aligned} \tag{26}$$

In the limit as $N \to \infty$, the summation converges to an integral

$$\begin{aligned} & I\left(t_{0,\text{ref}}\right) \\ & = \bar{\sigma} \int_{-\infty}^{\infty} \operatorname{sinc}\left(KT\tau\right) \operatorname{sinc}\left[KT\left(\tau + t_{\text{mis}}\right)\right] \\ & \qquad \exp\left\{j2\pi\left[-f_0 t_b - \Delta f\tau\right]\right\} d\tau \\ & = \bar{\sigma} \exp\left\{-j2\pi f_0 t_b\right\} \\ & \qquad \int_{-\infty}^{\infty} \operatorname{sinc}\left(KT\tau\right) \operatorname{sinc}\left[KT\left(\tau + t_{\text{mis}}\right)\right] \exp\left\{-j2\pi\Delta f\tau\right\} d\tau \end{aligned} \tag{27}$$

where $\bar{\sigma}$ is the RCS density in range. The integral is a Fourier transform and can be calculated as follows:

$$\begin{aligned} & f\left(\Delta f\right) \\ & = \int_{-\infty}^{\infty} \operatorname{sinc}\left(KT\tau\right) \operatorname{sinc}\left[KT\left(\tau + t_{\text{mis}}\right)\right] \exp\left\{-j2\pi\Delta f\tau\right\} d\tau \end{aligned}$$

Authorized licensed use limited to: Peking University. Downloaded on March 05,2026 at 17:19:39 UTC from IEEE Xplore. Restrictions apply.

$$
\begin{aligned}
&= \mathcal{F}\left[\operatorname{sinc}\left(KT\tau\right)\right] \otimes \mathcal{F}\left\{\operatorname{sinc}\left[KT\left(\tau + t_{\text{mis}}\right)\right]\right\} \\
&= \operatorname{rect}\left(\frac{\Delta f}{KT}\right) \otimes \operatorname{rect}\left(\frac{\Delta f}{KT}\right) \exp\left\{j2\pi\Delta f t_{\text{mis}}\right\} \\
&= \int_{-\infty}^{\infty} \operatorname{rect}\left(\frac{g}{KT}\right) \exp\left\{j2\pi t_{\text{mis}} g\right\} \operatorname{rect}\left(\frac{\Delta f - g}{KT}\right) dg \\
&= \frac{\sin\left[\pi t_{\text{mis}}\left(|K|T - |\Delta f|\right)\right]}{\pi t_{\text{mis}}} \exp\left\{j2\pi\Delta f \frac{t_{\text{mis}}}{2}\right\}
\end{aligned} \tag{28}
$$

where $\otimes$ denotes the convolution operation and $\operatorname{rect}(x)$ is the rectangular function defined as

$$
\operatorname{rect}\left(x\right) = \begin{cases} 1, & \text{if } |x| \le 0.5 \\ 0, & \text{otherwise.} \end{cases} \tag{29}
$$

We now elaborate on the derivation of the final line of (28). The expression in the preceding line represents an inverse Fourier transform, whose integration limits are defined by the two rectangular functions

$$
\begin{aligned}
\text{upper limit} = g_{\text{upper}} &= \min\left(\frac{|K|T}{2}, \Delta f + \frac{|K|T}{2}\right) \\
&= \begin{cases} \dfrac{|K|T}{2}, & \text{if } \Delta f \ge 0 \\ \Delta f + \dfrac{|K|T}{2}, & \text{if } \Delta f < 0 \end{cases}
\end{aligned} \tag{30}
$$

$$
\begin{aligned}
\text{lower limit} = g_{\text{lower}} &= \max\left(-\frac{|K|T}{2}, \Delta f - \frac{|K|T}{2}\right) \\
&= \begin{cases} \Delta f - \dfrac{|K|T}{2}, & \text{if } \Delta f \ge 0 \\ -\dfrac{|K|T}{2}, & \text{if } \Delta f < 0. \end{cases}
\end{aligned} \tag{31}
$$

After applying these limits, the integral simplifies to

$$
\begin{aligned}
f\left(\Delta f\right) &= \int_{g_{\text{lower}}}^{g_{\text{upper}}} \exp\left\{j2\pi t_{\text{mis}} g\right\} dg \\
&= \frac{\sin\left[\pi t_{\text{mis}}\left(|K|T - |\Delta f|\right)\right]}{\pi t_{\text{mis}}} \exp\left\{j2\pi t_{\text{mis}} \frac{\Delta f}{2}\right\}.
\end{aligned} \tag{32}
$$

Substituting (28) into (27), the interferogram becomes

$$
\begin{aligned}
I\left(t_{0,\text{ref}}\right) = \bar{\sigma} &\frac{\sin\left[\pi t_{\text{mis}}\left(|K|T - |\Delta f|\right)\right]}{\pi t_{\text{mis}}} \\
&\exp\left\{j2\pi\left(-f_0 t_b + \Delta f \frac{t_{\text{mis}}}{2}\right)\right\}.
\end{aligned} \tag{33}
$$

In the absence of the misregistration ($t_{\text{mis}} = 0$), the interferogram is

$$
I_0\left(t_{0,\text{ref}}\right) = \bar{\sigma}\left(|K|T - |\Delta f|\right) \exp\left\{-j2\pi f_0 t_b\right\} \tag{34}
$$

whose phase comprises solely the InSAR topographic phase. After removing this topographic phase from (33), the residual phase thus constitutes the phase error due to misregistration

$$
\begin{aligned}
\varphi_{\text{error}} &= \arg\left(I\right) - \arg\left(I_0\right) \\
&= 2\pi\Delta f \frac{t_{\text{mis}}}{2} \\
&= \frac{4\pi}{c}\Delta f \frac{r_{\text{mis}}}{2}
\end{aligned} \tag{35}
$$

where $r_{\text{mis}} = ct_{\text{mis}}/2$. The result is the same as (8).

## ACKNOWLEDGMENT

The ALOS-2 data were provided by Japan Aerospace Exploration Agency (JAXA) through the ALOS-4 Calibration/Validation and Science Team Project under Grant ER4A2N005. This article contains modified Copernicus Sentinel data. The authors thank the reviewers for the very constructive comments that substantially improve this article.

## REFERENCES

[1] E. Rodriguez and J. M. Martin, "Theory and design of interferometric synthetic aperture radars," *IEE Proc. F Radar Signal Process.*, vol. 139, no. 2, pp. 147–159, Apr. 1992, doi: 10.1049/ip-f-2.1992.0018.

[2] D. Massonnet and K. L. Feigl, "Discrimination of geophysical phenomena in satellite radar interferograms," *Geophys. Res. Lett.*, vol. 22, no. 12, pp. 1537–1540, Jun. 1995, doi: 10.1029/95gl00711.

[3] R. Goldstein, "Atmospheric limitations to repeat-track radar interferometry," *Geophys. Res. Lett.*, vol. 22, no. 18, pp. 2517–2520, Sep. 1995, doi: 10.1029/95gl02475.

[4] H. Tarayre and D. Massonnet, "Atmospheric propagation heterogeneities revealed by ERS-1 interferometry," *Geophys. Res. Lett.*, vol. 23, no. 9, pp. 989–992, May 1996, doi: 10.1029/96gl00622.

[5] P. A. Rosen, S. Hensley, H. A. Zebker, F. H. Webb, and E. J. Fielding, "Surface deformation and coherence measurements of Kilauea Volcano, Hawaii, from SIR-C radar interferometry," *J. Geophys. Res., Planets*, vol. 101, no. E10, pp. 23109–23125, Oct. 1996, doi: 10.1029/96je01459.

[6] H. A. Zebker, P. A. Rosen, and S. Hensley, "Atmospheric effects in interferometric synthetic aperture radar surface deformation and topographic maps," *J. Geophys. Res., Solid Earth*, vol. 102, no. B4, pp. 7547–7563, Apr. 1997, doi: 10.1029/96jb03804.

[7] C. Gisinger et al., "In-depth verification of Sentinel-1 and TerraSAR-X geolocation accuracy using the Australian corner reflector array," *IEEE Trans. Geosci. Remote Sens.*, vol. 59, no. 2, pp. 1154–1181, Feb. 2021, doi: 10.1109/TGRS.2019.2961248.

[8] R. Scheiber and A. Moreira, "Coregistration of interferometric SAR images using spectral diversity," *IEEE Trans. Geosci. Remote Sens.*, vol. 38, no. 5, pp. 2179–2191, Sep. 2000, doi: 10.1109/36.868876.

[9] N. B. D. Bechor and H. A. Zebker, "Measuring two-dimensional movements using a single InSAR pair," *Geophys. Res. Lett.*, vol. 33, no. 16, Aug. 2006, Art. no. L16311, doi: 10.1029/2006gl026883.

[10] E. Sansosti, P. Berardino, M. Manunta, F. Serafino, and G. Fornaro, "Geometrical SAR image registration," *IEEE Trans. Geosci. Remote Sens.*, vol. 44, no. 10, pp. 2861–2870, Oct. 2006, doi: 10.1109/TGRS.2006.875787.

[11] R. Bamler and M. Eineder, "Accuracy of differential shift estimation by correlation and split-bandwidth interferometry for wideband and Delta-k SAR systems," *IEEE Geosci. Remote Sens. Lett.*, vol. 2, no. 2, pp. 151–155, Apr. 2005, doi: 10.1109/LGRS.2004.843203.

[12] F. De Zan and A. Monti Guarnieri, "TOPSAR: Terrain observation by progressive scans," *IEEE Trans. Geosci. Remote Sens.*, vol. 44, no. 9, pp. 2352–2360, Sep. 2006, doi: 10.1109/TGRS.2006.873853.

[13] C. Liang and E. J. Fielding, "Measuring azimuth deformation with L-band ALOS-2 ScanSAR interferometry," *IEEE Trans. Geosci. Remote Sens.*, vol. 55, no. 5, pp. 2725–2738, May 2017, doi: 10.1109/TGRS.2017.2653186.

[14] P. Prats-Iraola, R. Scheiber, L. Marotti, S. Wollstadt, and A. Reigber, "TOPS interferometry with TerraSAR-X," *IEEE Trans. Geosci. Remote Sens.*, vol. 50, no. 8, pp. 3179–3188, Aug. 2012, doi: 10.1109/TGRS.2011.2178247.

[15] N. Yague-Martinez, P. Prats-Iraola, S. Wollstadt, and A. Moreira, "The 2-Look TOPS mode: Design and demonstration with TerraSAR-X," *IEEE Trans. Geosci. Remote Sens.*, vol. 57, no. 10, pp. 7682–7703, Oct. 2019, doi: 10.1109/TGRS.2019.2915797.

[16] D. Just and R. Bamler, "Phase statistics of interferograms with applications to synthetic aperture radar," *Appl. Opt.*, vol. 33, no. 20, pp. 4361–4368, Jul. 1994, doi: 10.1364/ao.33.004361.

[17] R. F. Hanssen, *Radar Interferometry: Data Interpretation and Error Analysis*. Norwell, MA, USA: Kluwer, 2002.

[18] F. De Zan, A. Parizzi, P. Prats-Iraola, and P. López-Dekker, "A SAR interferometric model for soil moisture," *IEEE Trans. Geosci. Remote Sens.*, vol. 52, no. 1, pp. 418–425, Jan. 2014, doi: 10.1109/TGRS.2013.2241069.

Authorized licensed use limited to: Peking University. Downloaded on March 05,2026 at 17:19:39 UTC from IEEE Xplore. Restrictions apply.

[19] F. De Zan, M. Zonno, and P. López-Dekker, "Phase inconsistencies and multiple scattering in SAR interferometry," *IEEE Trans. Geosci. Remote Sens.*, vol. 53, no. 12, pp. 6608–6616, Dec. 2015, doi: 10.1109/TGRS.2015.2444431.

[20] S. Zwieback et al., "A statistical test of phase closure to detect influences on DInSAR deformation estimates besides displacements and decorrelation noise: Two case studies in high-latitude regions," *IEEE Trans. Geosci. Remote Sens.*, vol. 54, no. 9, pp. 5588–5601, Sep. 2016, doi: 10.1109/TGRS.2016.2569435.

[21] Y. Zheng, H. Fattahi, P. Agram, M. Simons, and P. Rosen, "On closure phase and systematic bias in multilooked SAR interferometry," *IEEE Trans. Geosci. Remote Sens.*, vol. 60, 2022, Art. no. 5226611, doi: 10.1109/TGRS.2022.3167648.

[22] Y. Maghsoudi, A. J. Hooper, T. J. Wright, M. Lazecky, and H. Ansari, "Characterizing and correcting phase biases in short-term, multilooked interferograms," *Remote Sens. Environ.*, vol. 275, Jun. 2022, Art. no. 113022, doi: 10.1016/j.rse.2022.113022.

[23] R. Jolivet et al., "Improving InSAR geodesy using global atmospheric models," *J. Geophys. Res., Solid Earth*, vol. 119, no. 3, pp. 2324–2341, Mar. 2014, doi: 10.1002/2013jb010588.

[24] J. Böhm and H. Schuh, *Atmospheric Effects in Space Geodesy*, 5th ed., Berlin, Germany: Springer, 2013.

[25] C. Liang, E. J. Fielding, Z. Liu, T. Motohka, R. Natsuaki, and S.-H. Yun, "An analysis of the potentials of L-band SAR satellites for measuring azimuth motion," *Remote Sens. Environ.*, vol. 315, Dec. 2024, Art. no. 114426.

[26] G. Gomba, F. De Zan, and S. Tong, "Seasonal and long-term vegetation effects on Sentinel-1 range coregistration shifts," in *Proc. ESA Living Planet Symp.*, Vienna, Austria, 2025, pp. 1–15.

[27] A. Freeman, "SAR calibration: An overview," *IEEE Trans. Geosci. Remote Sens.*, vol. 30, no. 6, pp. 1107–1121, Nov. 1992, doi: 10.1109/36.193786.

[28] C. Liang and E. J. Fielding, "Interferometry with ALOS-2 full-aperture ScanSAR data," *IEEE Trans. Geosci. Remote Sens.*, vol. 55, no. 5, pp. 2739–2750, May 2017, doi: 10.1109/TGRS.2017.2653190.

[29] I. G. Cumming and F. H. Wong, *Digital Processing of Synthetic Aperture Radar Data: Algorithms and Implementation*. Norwood, MA, USA: Artech House, 2005.

[30] T. G. Farr et al., "The shuttle radar topography mission," *Rev. Geophys.*, vol. 45, no. 2, Jun. 2007, Art. no. RG2004, doi: 10.1029/2005rg000183.

[31] P. Rizzoli et al., "Generation and performance assessment of the global TanDEM-X digital elevation model," *ISPRS J. Photogramm. Remote Sens.*, vol. 132, pp. 119–139, Oct. 2017, doi: 10.1016/j.isprsjprs.2017.08.008.

[32] V. Leister-Taylor et al., *Copernicus DEM Validation Report*, document GEO.2018-1988-2, Nov. 9, 2020. [Online]. Available: https://dataspace.copernicus.eu/explore-data/data-collections/copernicus-contributing-missions/collections-description/COP-DEM

[33] Z. Yunjun et al., "Range geolocation accuracy of C-/L-band SAR and its implications for operational stack coregistration," *IEEE Trans. Geosci. Remote Sens.*, vol. 60, 2022, Art. no. 5227219, doi: 10.1109/TGRS.2022.3168509.

[34] P. A. Rosen, E. Gurrola, G. F. Sacco, and H. Zebker, "The InSAR scientific computing environment," in *Proc. EUSAR; 9th Eur. Conf. Synth. Aperture Radar*, Nuremberg, Germany, Apr. 2012, pp. 730–733.

[35] D. Sandwell, R. Mellors, X. Tong, M. Wei, and P. Wessel, "Open radar interferometry software for mapping surface deformation," *Eos, Trans. Amer. Geophys. Union*, vol. 92, no. 28, p. 234, Jul. 2011, doi: 10.1029/2011eo280002.

[36] M. Nannini et al., "Advancements in PRISM: DLR processing framework for interferometric SAR missions," in *Proc. 15th Eur. Conf. Synth. Aperture Radar (EUSAR)*, Munich, Germany, Mar. 2024, pp. 833–838.

[37] F. Gatelli, A. M. Guamieri, F. Parizzi, P. Pasquali, C. Prati, and F. Rocca, "The wavenumber shift in SAR interferometry," *IEEE Trans. Geosci. Remote Sens.*, vol. 32, no. 4, pp. 855–865, Jul. 1994, doi: 10.1109/36.298013.

[38] C. Oliver and S. Quegan, "Principles of SAR image formation," in *Understanding Synthetic Aperture Radar Images*, vol. 6. Rijeka, Croatia: SciTech, 2004, ch. 2, sec. 2, pp. 11–42.

[39] H. Ansari, F. De Zan, and A. Parizzi, "Study of systematic bias in measuring surface deformation with SAR interferometry," *IEEE Trans. Geosci. Remote Sens.*, vol. 59, no. 2, pp. 1285–1301, Feb. 2021, doi: 10.1109/TGRS.2020.3003421.

[40] F. De Zan and G. Gomba, "Vegetation and soil moisture inversion from SAR closure phases: First experiments and results," *Remote Sens. Environ.*, vol. 217, pp. 562–572, Nov. 2018, doi: 10.1016/j.rse.2018.08.034.

[41] E. Wig, R. Michaelides, and H. Zebker, "Fine-resolution measurement of soil moisture from cumulative InSAR closure phase," *IEEE Trans. Geosci. Remote Sens.*, vol. 62, 2024, Art. no. 5212315, doi: 10.1109/TGRS.2024.3399069.

[42] H. Fattahi, P. Agram, and M. Simons, "A network-based enhanced spectral diversity approach for TOPS time-series analysis," *IEEE Trans. Geosci. Remote Sens.*, vol. 55, no. 2, pp. 777–786, Feb. 2017, doi: 10.1109/TGRS.2016.2614925.

[43] H. Fattahi, M. Simons, and P. Agram, "InSAR time-series estimation of the ionospheric phase delay: An extension of the split range-spectrum technique," *IEEE Trans. Geosci. Remote Sens.*, vol. 55, no. 10, pp. 5984–5996, Oct. 2017.

[44] C. Gisinger et al., "The extended timing annotation dataset for Sentinel-1—Product description and first evaluation results," *IEEE Trans. Geosci. Remote Sens.*, vol. 60, 2022, Art. no. 5232622, doi: 10.1109/TGRS.2022.3194216.

**Fan Yang** received the B.S. degree in geographic information science from Peking University, Beijing, China, in 2022, where she is currently pursuing the Ph.D. degree in photogrammetry and remote sensing.

Her research interests include interferometric synthetic aperture radar (InSAR) and its applications in geoscience and natural hazards response.

**Cunren Liang** received the B.S. degree from Shandong University of Science and Technology, Qingdao, China, in 2008, and the Ph.D. degree from Peking University, Beijing, China, in 2014.

He is currently an Assistant Professor at Peking University. Previously, he was a Staff Scientist at California Institute of Technology (Caltech), Pasadena, CA, USA, from 2018 to 2021. Prior to joining Caltech, he was a NASA Post-Doctoral Program Fellow at Jet Propulsion Laboratory (JPL), Pasadena, from 2015 to 2018. His research interests are mainly in the field of microwave remote sensing, e.g., synthetic aperture radar (SAR) signal processing, interferometry SAR (InSAR), microwave scattering mechanism, and their applications in geosciences.

Dr. Liang is a member of American Geophysical Union. He was a recipient of the NASA Group Achievement Award in 2016 and the JPL Outstanding Postdoctoral Research Award in 2017.

**Yuhang Wang** received the B.S. degree in geographic information science from Peking University, Beijing, China, in 2023, where he is currently pursuing the Ph.D. degree in photogrammetry and remote sensing.

His research interests include the technical development of synthetic aperture radar (SAR) processing, interferometric SAR (InSAR), and InSAR applications in geoscience and natural hazards response.

Authorized licensed use limited to: Peking University. Downloaded on March 05,2026 at 17:19:39 UTC from IEEE Xplore. Restrictions apply.